Analysis and modeling of bubble-induced agitation from direct numerical simulation of homogeneous bubbly flows

A. du Cluzeau [1,*] G. Bois [1,†] N. Leoni,[1] and A. Toutant [2]

[1]*DEN–Service de thermo-hydraulique et de mécanique des fluides (STMF), CEA, Université Paris-Saclay, F-91191 Gif-sur-Yvette, France*

[2]*PROMES-CNRS (UPR 8521), Université de Perpignan Via Domitia, 66100 Perpignan, France*

(Received 12 October 2021; accepted 1 April 2022; published 20 April 2022)

In this study based on direct numerical simulations (DNS) of homogeneous bubbly flows, an analysis of velocity fluctuations is performed and a methodology for the development of a bubble-induced agitation (or pseudoturbulence) model is described. This process is based on the separation of two phenomena causing velocity fluctuations in the liquid: the agitation resulting from wakes and their collective interactions [wake-induced agitation (WIA)], which is our main focus, and the nonturbulent fluctuations resulting from averaged wakes and potential flows around bubbles [potential flow and averaged wake fluctuations (PWFs)]. We run DNS of fixed bubbles, with random spatial distribution, and compare the results to free-bubble simulations in order to build a model for those phenomena. The simulation of motionless bubbles allow the decomposition of the Reynolds stress transport equation to study WIA and PWFs separately. Then the main characteristics of bubbly flows are analyzed. The signature of an energy conversion from wake kinetic energy (PWFs) to turbulent kinetic energy (WIA) is observed, revealing the importance of nonlinear interactions and transfers between PWFs and WIA. A first proposal of model is made, which gives satisfactory results on our database for a wide range of bubble Reynolds numbers and is consistent with experimental observations. It is operational and can be implemented and assessed in an averaged code.

DOI: 10.1103/PhysRevFluids.7.044604

I. INTRODUCTION

Fluctuations in two-phase flows are historically divided into bubble-induced agitation (BIA) and shear-induced turbulence (SIT) [1] (see Fig. 1). SIT arises from the averaged shear produced for instance in near-wall regions. It is frequently seen as "turbulence in the absence of bubbles" whereas BIA represents the contribution added by the bubbles. In the broader context of multiphase flows (gas-particle and liquid-particle flows, droplets, etc.), BIA is often called *pseudoturbulence*, as its characteristic quantities are linked to the bubble's dynamics (slip velocity, bubble diameter). Following the work of [2], we employ the term *bubble-induced agitation* as it presents some features that differ from standard turbulence, which we detail below. To emphasize in particular the fact that part of the fluctuations induced by the bubbles' agitation is nothing alike turbulence, note that BIA and SIT have different characteristic length scales. For turbulence modeling, this distinction is crucial because it will determine whether or not the length scale must be modeled using a transport equation (e.g., dissipation rate) or not (i.e., for pseudoturbulence).

*antoine.ducluzeau@cea.fr
†guillaume.bois@cea.fr

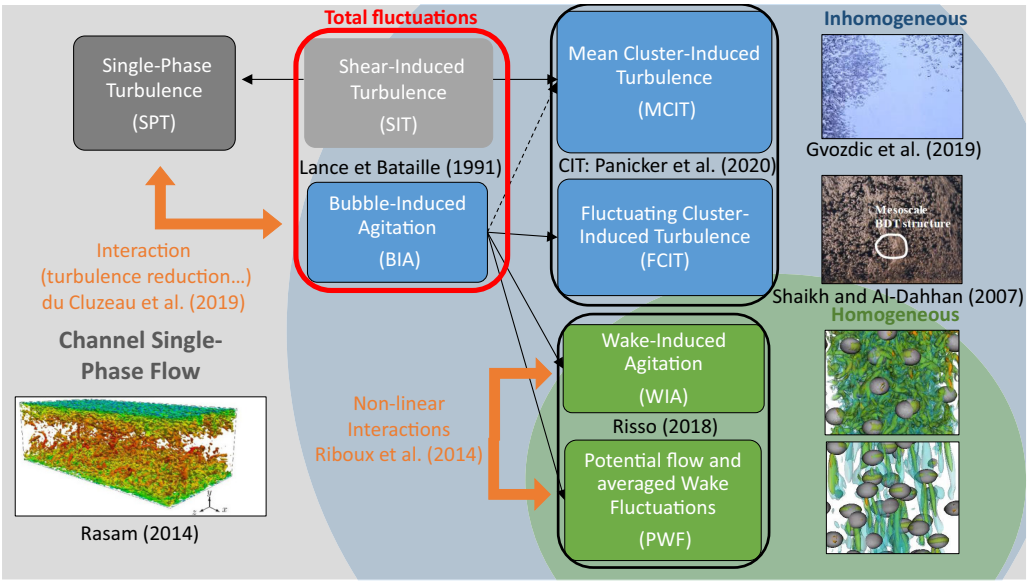

FIG. 1. Scheme of the agitation mechanisms in bubbly flows. The red box represents the foundational work of Lance and Bataille [1]. Black boxes contain concepts often studied together. The black and orange arrows respectively symbolize a decomposition and an interaction. Green = homogeneous bubbly flows; blue+green = inhomogeneous bubbly flows; gray+blue+green = ordinary bubbly flow [1,3–8].

Note that SIT can also be generated by an inhomogeneous distribution of bubbles at high void fraction. For instance, the velocity difference between populated and empty regions can produce averaged or local shear which generates turbulence. This phenomenon is studied in the literature as buoyancy-driven turbulence (BDT) because "The high gas fraction bubbly flow regime or heterogeneous regime is prone to buoyancy-induced instabilities, which lead to the formation of heterogeneous bubble flows producing buoyancy driven turbulence" [4]. Nonetheless, all the velocity fluctuations generated by bubbles are buoyancy-induced, including those not related to inhomogeneities. Thus, the name cluster-induced turbulence (CIT) is also used in Ref. [9] (see Fig. 1) for such fluctuations.

Moreover, the BIA/SIT separation implies that BIA is not related to shear. Instead, CIT is the consequence of a shear generated by bubbles. Being caused by both bubbles and shear, CIT can be arbitrarily interpreted as SIT or BIA. To scrupulously separate the agitation linked to bubbles from single-phase turbulence, it is perhaps clearer to speak of single-phase turbulence (SPT) and bubble-induced agitation (BIA). Note that there is strong interaction between both, for example via the phenomenon of turbulence reduction [10–13].

In case of a homogeneous distribution of bubbles (low to moderate void fractions), Ref. [2] proposed a splitting of BIA into spatial and temporal agitations. The spatial agitation corresponds to the coherent structures around bubbles such as the averaged wake and the potential flow [14–16]. In the present study, it is coined as potential flow and averaged-wake fluctuations (PWFs). These fluctuations, although stationary in the reference frame of bubbles, are responsible for a part of the dissipation process in the wakes and interact in a strongly nonlinear manner with the second contribution coined as wake-induced agitation (WIA). WIA is linked to wake instabilities on the one hand and to the collective interaction of wakes on the other. Wake instabilities generate temporal fluctuations as von Kármán alleys; it should be noted that this part of fluctuations is not necessarily turbulent, as it does not necessarily lead to an energy cascade and to a dissipative process at the molecular scale. For this reason, the terminology "agitation" is more suited than

"turbulence." However, Refs. [7,8,11,17] demonstrate that the collective interaction of wakes is a turbulent process. Therefore, WIA combines two phenomena.

To apply these concepts to an averaged model (i.e., the Euler-Euler two-fluid model with interpenetrating media), additional distinctions have to be made. If SIT is the turbulence generated by the averaged shear, it makes up part of the CIT (because inhomogeneities caused by clusters induce shear). The larger scales of inhomogeneities (and steady inhomogeneities) are captured by an averaged model, contrary to homogeneity fluctuations (for instance, within a bubble plume) that require modeling. From the modeling point of view, this distinction is important even if the physical mechanism is unchanged. In Fig. 1 we refer to mean cluster-induced turbulence (MCIT) as the part resolved intrinsically by a Reynolds averaged model, and to fluctuating cluster-induced turbulence (FCIT) for the part which requires additional modeling. This efficient agitation is significant at high void fraction (this is not the case in the present study). The other fluctuations (WIA, PWFs) take place at the bubble scale. In contrast with WIA and PWFs that need to be modeled for any two-fluid approach, CIT can be either resolved in a two-fluid model that resolves shear and buoyancy-induced turbulence or modeled in a two-fluid turbulence model that considers statistically a broader range of scales. In this paper, the focus will be set upon the WIA and PWF modeling.

A proposal is made in Fig. 1 to give names and abbreviations with a clear separation of the effects mentioned above. Total fluctuations R_{ij} are defined as the sum of SPT and BIA, and MCIT is considered only as a product of BIA. In both theory and practice, it is easier to consider SIT as the combination of both SPT and MCIT. Consequently, there remain only three parts to the BIA (namely, FCIT, WIA, and PWFs) even though MCIT cannot exist without bubbles (and is therefore bubble-induced too as indicated by the dashed arrow in Fig. 1). Finally, we consider fluctuations as

$$R_{ij} = R_{ij}^{SIT} + R_{ij}^{BIA}, \tag{1}$$

$$R_{ij}^{SIT} = R_{ij}^{SPT} + R_{ij}^{MCIT}, \tag{2}$$

$$R_{ij}^{BIA} = R_{ij}^{FCIT} + R_{ij}^{WIA} + R_{ij}^{PWF}. \tag{3}$$

Today, models used by industrial codes are far from taking into account the whole complexity of two-phase bubbly flows and most of these studies stand for the development of models that include more physical phenomena. Models for bubbly flows are generally *ad hoc* extension of single-phase methods ($k-\epsilon$, RSM, etc.). Ignoring the specificity of BIA (with respect to single-phase turbulence), interfacial production becomes an additional source term in the transport equation of kinetic energy [18–20]. Classical models involve only the splitting of turbulence into SIT and BIA. In order to adapt single-phase turbulence models to two-phase flows, many authors have implicitly assumed that FCIT, WIA, and PWFs may be modeled together [18,19]. The reader is referred to the review [20]. Generally, the most common models in CFD use an additional production term in the turbulent energy transport equation related to the bubble impact, and add a sink term in the dissipation equation to take into account the additional dissipation induced by bubble wakes [21]. The latter is simply taken as the additional interfacial production introduced in the turbulent kinetic energy transport equation scaled by a characteristic timescale. This timescale be either expressed as the turbulence integral timescale $\tau = k/\epsilon$, which amounts to the SPT scale, or follow a more advanced formulation based on a blending of the turbulence integral timescale and the bubble/turbulence interaction timescale [22]. Mostly, the velocity fluctuations, bubble-generated or not, are dissipated with a single characteristic frequency generally based on single-phase turbulence. These models are thus suitable for high-Reynolds number simulations, in which the impact of BIA can be negligible. For low-Reynolds flows, large improvements are still possible.

Although there have been several attempts to use other decompositions based on physical considerations, to the best of our knowledge, most of the turbulence models are still based on a coarse vision of two-phase flow. We can note some exceptions like the work of [23], who proposed to distinguish the dissipative and nondissipative parts of BIA. More recently, Ref. [4] offered an

adaptation of the two-fluid model centered on FCIT modeling. Thus, a "classical" two-fluid model can generally resolve SIT (and potentially FCIT), but it does not resolve BIA (or pseudoturbulence) without a specific attention. Thus, the BIA model proposed in this article could be used in any two-fluid model, including one that already resolves other parts of turbulence.

To the best of our knowledge, Chahed's model [23] is yet the only model in the two-phase flow literature to offer a distinction between PWFs and WIA. The challenge of the present paper is to analyze the physics, propose a methodology in order to develop models and give a first proposal. For this, we study the case of homogeneous bubbly flows at low void fractions. The idea for homogeneous conditions as considered here is to model the whole DNS by a single cell. Thus, local variations are statistically averaged. The analysis reveals that the homogeneous assumption stands, even when variations of volume fraction are observed in the computational domain. In this configuration, there is neither MCIT nor FCIT (or negligible), and the agitation of the liquid phase contains mostly WIA and PWFs (see Fig. 1).

Dissociating WIA and PWFs is an arduous task, as it often relies on calculations in the reference frame of bubbles (see [8,17,24] for more details). The experiment proposed in Ref. [8] makes it possible to separate these two contributions by studying the turbulent fluctuations behind a swarm of bubbles. Alternative works [14,15] succeeded in studying PWFs alone in a Hele-Shaw cell by preventing the appearance of WIA with a strong containment. Amoura, Besnaci, and Risso [17] also observed that nonlinear interactions leading to WIA production do not occur for bubble Reynolds numbers $\mathrm{Re}_b = \rho_l d_b u_r/\mu_l$ less than 200. In [13], for small bubble Reynolds numbers encountered in low gravity conditions, BIA is composed of PWFs exclusively, thus allowing the study of PWFs through the analysis of its Reynolds stress transport equation. These techniques enable only the study of PWFs alone, but in the current state of knowledge, the only way to isolate WIA is the fixed-bubble configuration. WIA cannot be studied in DNS of channel flows because it is inseparable from SIT. Hence, following Ref. [17], we propose in this article a configuration in which WIA and PWFs can be studied more rigorously than in a plane channel: the comparison of freely evolving bubbles to the fixed random equivalent distribution. In addition, studying bubbly flows in the reference frame attached to the bubbles allows the separation of WIA and PWFs [8,17], to the purpose of separate effect analysis. The counterpart of this method is the inherent suppression of the relative motion between bubbles and its effect. Several numerical studies have already addressed similar configurations with regular arrays of fixed solid spheres [25] or bubbles [26]. We propose here the study of fixed bubbles with random spatial distribution.

As suggested by numerical works [13,27–29], budgets of averaged equations can be used to improve turbulence modeling. The Reynolds stresses transport equation for two-phase flows [21,30] contains, in addition to classical terms (production, dissipation, etc.), an interfacial production term related to the kinetic energy transfer between liquid and vapour phases at the bubble interface. Even with optical methods, the measurement of this interfacial production involving interfacial pressures and interfacial velocities is hardly attainable with the current measuring techniques [31,32]. On the other hand, this quantity can be measured from DNS numerical experiments [29,33], leading to an improvement of turbulence models [22,27–29,34–40].

We wish here to reiterate the attempt in Ref. [23] to propose a BIA model separating the transport equation of the Reynolds stresses into two contributions. We propose to build an agitation model for homogeneous bubbly flows from the DNS study. For such a flow, the Reynolds stresses transport equation can be written as

$$R_{ij}^{BIA} = R_{ij}^{WIA} + R_{ij}^{PWF}, \tag{4}$$

$$\frac{D\alpha_l R_{ij}^{WIA}}{Dt} = \phi_{ij}^{WIA} - 2\epsilon_{ij}^{WIA} + \Pi_{ij}^{WIA} - T_{ij}, \tag{5}$$

$$\frac{D\alpha_l R_{ij}^{PWF}}{Dt} = \phi_{ij}^{PWF} - 2\epsilon_{ij}^{PWF} + \Pi_{ij}^{PWF} + T_{ij}, \tag{6}$$

where PWFs and WIA have their own transport equations. The theory behind this decomposition is presented in Sec. III. $\frac{D}{Dt}$ is the material derivative and α_l is the liquid volume fraction. R, Π, ϕ, ϵ, and T are, respectively, the Reynolds stress, interfacial production, redistribution, dissipation, and energy transfer from WIA to PWFs. Because of the zero averaged shear in a flow of homogeneous bubbles, there are no production and diffusion operators.

It may be surprising to express the evolution of PWFs with a transport equation. Indeed, these fluctuations are stationary in the reference frame of bubbles. They result from the potential flow and the average wake around them; there is nothing turbulent in this phenomenon [41,42]. Despite this, these fluctuations are a part of the Reynolds stress in bubbly flows. Thus, they follow the same transport equation, but the physical interpretation of the different terms must be revised. It should be noted that models for PWFs already exist in Refs. [13,16] (with algebraic relation from Wijngaarden [43]). Other methodologies propose to model this part of the velocity fluctuations as an additional viscosity (see [42,44]). The present study will then be focused on the modeling of WIA.

The article is structured as follows. Section II presents the DNS and the numerical method, in particular the forcing of the bubble positions for fixed-bubble simulations. To define the different terms of Eqs. (5) and (6), we explain in Sec. III how the flow configuration of fixed bubbles allows a rigorous writing of the Reynolds stress transport equations for PWFs and WIA separately. Then each of these terms is estimated using our DNS database. Section IV analyzes the main characteristics of bubbly flows and compares free-bubble with fixed-bubble configurations. It is followed by a statistical analysis of WIA and PWFs. The purpose of this part is to verify the statistical properties of fluctuations generated by the bubbles and to understand the impact of fixing them. Section V uses fixed and free bubbly flows to complete a first modeling of the WIA transport equation (5).

II. DIRECT NUMERICAL SIMULATIONS

This section presents the simulations of bubbly flows (fixed and free), their physical and numerical parameters, as well as the numerical methods used to fix bubbles and to find the flow rates corresponding to the statistically stationary states.

A. Physical setup

Physical behavior of two-phase bubbly flows is strongly related to local phenomena occurring in bubble surroundings. Classical experiments struggle to isolate their individual roles, justifying the use of DNS as a numerical experiment. In the present work, ten calculations of bubbly flows are studied. The computational domain is $2 \times 0.5 \times 0.5$ [cm]. Periodic boundary conditions are set on the axial (x, streamwise) and transversal (y, z, spanwise) directions. An influence of the size of the computational domain can be expected to some extent (artificial length scales may be induced by the computational box), especially at low Reynolds numbers. However, for particle-resolved DNS, a compromise must be achieved due to computational limits. The domain size and number of bubbles considered are similar to the current state of the art [29,34,45]. Pandey, Ramadugu, and Perlekar [45] argue that these dimensions are sufficient to prevent the wake from interacting with itself. Moreover, the effect of the domain size is expected to be of minor consequence on the purpose of this article, where most of the modeling is performed by comparing cases with identical domains and meshes. The tendencies illustrated in the article are mostly illustrative of the physical insight gained by this analysis. Trends, behaviors, and relative magnitudes are commented. They are expected to remain true with finer or larger simulations.

The flow is initially at rest before being driven by the action of buoyancy. We simulate a population of 57 bubbles ($d_b = 1$ mm) with a void fraction of 6%. Because of the moderate void fraction in our simulations, coalescence is neglected. Breakup is not observed for the range of Eötvös and bubble Reynolds numbers considered. Since the present focus is on dynamical aspects, the flow is considered isothermal with no phase change and constant physical properties for each phase.

TABLE I. Common parameters to all bubbly flow calculations (fixed and free). g, d_b, N_b, σ, α_v, μ, and ρ are, respectively, the gravity, bubble diameter, number of bubbles, surface tension, void fraction, viscosity, and density. The common Eötvös number is then Eo = 0.59. μ_l varies depending on the case (see Table II)

g [m/s^2]	d_b [mm]	N_b	ρ_l/ρ_v [kg/m^3]	α_v	σ [N/m]	μ_v [Pa s]	Domain ($\times 10^{-2}$ m)
9.81	1	57	1171/87	6%	0.018	1.35×10^{-5}	$2 \times 0.5 \times 0.5$

Initially, bubbles are randomly distributed in the domain. Then two different configurations are considered:

(1) Fixed-bubble simulations: bubbles are held at their initial positions by the addition of an external force. The downward motion of the liquid phase creates the relative velocity between phases. These simulations neglect the chaotic motion of bubbles, namely, their relative movements with respect to each other. In addition, they assume a relatively homogeneous distribution of bubbles. These cases allow WIA/PWF separation.

(2) Free-bubble simulations: bubbles are free to move under the action of buoyancy and other interfacial forces. No hypothesis is made on the distribution nor on bubble movement. In this configuration, WIA/PWF separation is complicated, if not impossible.

The physical properties of the liquid and gas listed in Table I are taken from the DEBORA experiments [46], in which liquid R12 Freon at 16 bar and at saturation temperature is used to represent a water/steam reactor flow at 100 bar (see R12 fluid at the NIST website [47]). In particular, this simulating fluid allows an approximate conservation of the density ratio between phases of a pressurized water reactor flow. We increase surface tension in order to prevent any fragmentation of bubbles (including by the effect of the control force).

In a bubbly flow, several parameters can impact the BIA: the bubble Reynolds number $\mathrm{Re}_b = \rho_l d_b u_r/\mu_l$, the Eötvös number $\mathrm{Eo} = g d_b^2(\rho_l - \rho_v)/\sigma$, and the void fraction α_v. We chose to carry out a parametric study on the bubble Reynolds number. To observe trends, ten calculations are proposed between $\mathrm{Re}_b = 100$ and $\mathrm{Re}_b = 800$ (five with fixed bubbles and five with free bubbles). Below $\mathrm{Re}_b = 100$, the flow is laminar. Beyond $\mathrm{Re}_b = 800$, Ref. [17] showed that statistical results converge to an asymptotic limit; moreover, such calculations require too much computational ressource. To vary the bubble Reynolds number, the liquid viscosity is modified from $\mu_l = 1.8 \times 10^{-4}$ Pa s up to $\mu_l = 1.5 \times 10^{-3}$ Pa s (see Table II for the different cases).

TABLE II. Simulation parameters. For each column, a fixed-bubble calculation and a free-bubble calculation are performed. The resolution used in all calculations is 25.6 cells per diameter. The relative velocity $u_r = \overline{U_v}^v - \overline{U_l}^l$ is a result of the simulations that varies slightly. $\overline{U_v}^v$ and $\overline{U_l}^l$ are the phase-averaged velocities in each phase. $u_r \approx 0.1$ m/s for free bubbles, $u_r \approx 0.13$ m/s for fixed bubbles. This difference is discussed in Sec. IV A. Then the Weber number $\mathrm{We} = \rho_l u_r^2 d_b/\sigma$ varies slightly in the range $\mathrm{We}_b \in [1.04, 1.6]$ for fixed bubbles and $\mathrm{We}_b \in [0.61, 0.79]$ for free bubbles.

μ_l[Pa s]	1.578×10^{-3}	7.058×10^{-4}	3.5289×10^{-4}	2.379×10^{-4}	1.886×10^{-4}
$\mathrm{Re}_b^{\mathrm{fixed}}$	118	229	438	630	786
$\mathrm{Re}_b^{\mathrm{free}}$	72	171	345	539	684
$\mathrm{We}_b^{\mathrm{fixed}}$	1.65	1.23	1.13	1.06	1.04
$\mathrm{We}_b^{\mathrm{free}}$	0.61	0.69	0.71	0.78	0.79

B. Numerical setup

TrioCFD through its Front-Tracking algorithm [48] resolves the one-fluid equations of Kataoka [49]:

$$\nabla \cdot \mathbf{U} = 0, \tag{7}$$

$$\frac{\partial \rho \mathbf{U}}{\partial t} + \nabla \cdot (\rho \mathbf{U}\mathbf{U}) = -\nabla P + \rho \mathbf{g} + \nabla \cdot \tau_{\mathbf{k}} + \sigma \kappa \mathbf{n}_v \delta^i, \tag{8}$$

where each of the one-fluid variables is defined as a mixture of phase variables: $\phi = \sum_k \chi_k \phi_k$. ϕ_k can be $\mathbf{U}_k$, ρ_k, μ_k, or P_k, respectively, the velocity, density, viscosity, or pressure in phase k. The viscous stress tensor is defined as $\tau_{\mathbf{k}} = \sum_k \mu_k \chi_k (\nabla \mathbf{U}_{\mathbf{k}} + \nabla^T \mathbf{U}_{\mathbf{k}})$. χ_k is the phase indicator function, which is equal to 1 in phase k and 0 otherwise. The transport equation is then $\partial \chi_v / \partial t + \mathbf{U}_i \cdot \nabla \chi_v = 0$, where $\mathbf{U}_i$ is the interfacial velocity of the front. Here, in the absence of phase change, the velocity is continuous across the interface and $\mathbf{U}_i = \mathbf{U}$. σ is the surface tension, $\kappa = -\nabla_S \cdot \mathbf{n}_v$ is the local curvature, usually negative for bubbles, and $\mathbf{n}_v$ is vector normal to the interface defined by $\nabla \chi_v = -\mathbf{n}_v \delta^i$, where δ^i is the Dirac impulse at the interface i.

Following the proposal of Tryggvason *et al.* [50], a front-tracking method [48] is used to solve this set of equations in the whole computational domain, including both the vapor and liquid phases. The interface is followed by moving connected marker points. The Lagrangian markers are advected by the velocity field then interpolated from the Eulerian grid. In order to preserve the mesh quality and to limit the need for remeshing operations, only the normal component of the velocity field is used in the marker transport. After the transport step, the front is used to update the phase indicator function, the density, and the viscosity at each Eulerian grid point. The Navier-Stokes equations are then solved by a projection method [51] using fourth-order central differentiation for evaluation of the convective and diffusive terms on a fixed, staggered cartesian grid. Fractional time stepping leads to a third-order Runge-Kutta scheme [52] (see [53]). In the two-step prediction-correction algorithm, a surface tension source is added to the main flow source term and to the evaluation of the convection and diffusion operators in order to obtain the predicted velocity (see [48]). Then, an elliptic pressure equation is solved by an algebraic multigrid method to impose a divergence-free velocity field. TrioCFD has already been widely used for two-phase [13,22,54–60] and single-phase [61–64] flow studies. Validations of the code are provided in Ref. [13].

The ensemble average is taken as an average in space and time, by application of the ergodicity hypothesis to periodic directions:

$$\overline{\phi} = \overline{\overline{\phi}^X}^T = \frac{1}{\Delta t_{\text{ave}}} \int_{t-\Delta t_{\text{ave}}/2}^{t+\Delta t_{\text{ave}}/2} \overline{\phi}^X \, d\tau \tag{9}$$

with

$$\overline{\phi}^X = \frac{1}{L_x L_y L_z} \int_0^{L_x} \int_0^{L_y} \int_0^{L_z} \phi \, dx \, dy \, dz, \tag{10}$$

where L_x, L_y, and L_z are, respectively, the length of the domain in the (x, y, z) direction. Δt_{ave} is the time interval of the average expressed in time unit $t.u. = L_x / \overline{u_r}$.

The mesh resolution should ideally integrate the smallest scales of bubble-induced turbulence. For bubbly flows, the Kolmogorov scale can be estimated using the relation: $\eta = (\nu^3/\epsilon)^{1/4}$ where ϵ is estimated by the power of the buoyancy force: $\epsilon = \alpha_v g \langle u_r \rangle$ [7]. According to this criterion, a greater bubble Reynolds number requires a greater resolution, because wakes become increasingly turbulent. However, the resolution required for high Reynolds numbers is too expensive in terms of numerical resources. The resolution used in the present calculations is 25.6 cells per bubble diameter (note that Ref. [45] used 24 cells/diameter with the front-tracking algorithm of the PARIS simulator up to $\text{Re}_b = 546$). We demonstrate that it is sufficient for $\text{Re}_b = 438$ (see Fig. 2). Consequently, a

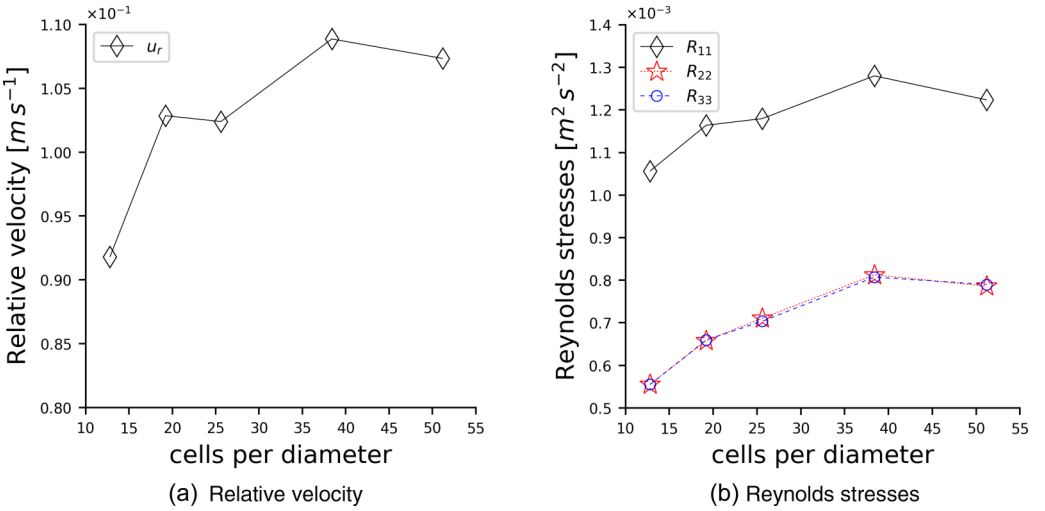

FIG. 2. Mesh convergence study for the relative velocity (a) and Reynolds stresses (b) for the case $\mathrm{Re}_b = 438$. The averaging time interval is 1 s after the steady-state establishment.

moderate deviation from converged results is possible for the cases at $\mathrm{Re}_b = 630$ and $\mathrm{Re}_b = 786$, which presumably require greater resources. We observe convergence of both first-order statistical quantities such as the relative velocity and second-order quantities such as the Reynolds stresses (see Fig. 2).

C. Control algorithms for fixed bubbles

For fixed-bubble simulations, an artificial control force is implemented in order to maintain bubbles at their initial positions. This tool is based on the work of Thomas *et al.* [65] who used a control force $\mathbf{F_i}$ on bubble i to measure interfacial forces. This force is applied as an additional source term on the vapor phase in the r.h.s. of Eq. (8) as

$$\mathbf{S_1} = \rho_v \sum_i \chi_{v,i} \mathbf{F_i}, \tag{11}$$

where $\chi_{v,i}$ and $\mathbf{F_i}$ are, respectively, the phase indicator function of the bubble i and the associated force. Therefore, $\mathbf{F_i}$ is an acceleration and its intensity can be compared to gravity. Thomas *et al.* [65] noted that bubbles have a stronger tendency to deformation with this force. It can be quantified by the instantaneous modified Eötvös number: $\mathrm{Eo}_i = \Delta\rho d_b^2(||\mathbf{g} + \mathbf{F_i}||)/\sigma$ where $||\mathbf{X}||$ is the norm of $\mathbf{X}$. At a given time, a fixed bubble subjected to turbulent motion may be impacted by significant control forces (of the order of magnitude of g). In our cases, for instance, the modified Eötvös number covers a range of $\mathrm{Eo}_i \in [0{:}2\mathrm{Eo}]$. The disturbance induced by the force $\mathbf{F_i}$ may lead to an unwanted destabilization of the interface. Anticipating this effect, the surface tension in the simulations has been increased to avoid fragmentation or excessive deformation. However, imposing an individual and time-dependent surface tension for each bubble is not permitted by our front-tracking algorithm, and it would be subject to difficult physical interpretation. In this study, the surface tension as been chosen heuristically to $\sigma = 0.018N/m$ to avoid bubble breakup. The same value is also taken for free bubbles. Preliminary simulations with the actual surface tension of Freon showed moderate deformations without breakup for free-bubble simulations. Surface-tension has been increased in order to avoid spurious deformations induced by the artificial spring force in fixed-bubble configurations. Then it seems a closer parallel if the surface tension is increased for

free cases too. The effect of stronger bubble deformations encountered for higher Eötvös or Weber numbers could be the focus of dedicated studies in the future.

The control force is defined at time step n for the bubble i as

$$\mathbf{F}_i^n = k_1\left(\mathbf{x}_i^n - \mathbf{x}_i^0\right) + k_2\frac{\mathbf{x}_i^n - \mathbf{x}_i^{n-1}}{\Delta t}, \tag{12}$$

where $\mathbf{x}^n$, $\mathbf{x}^{n-1}$, and $\mathbf{x}^0$ are, respectively, the positions of the center of mass of the bubble i at time steps n, $n-1$ and at the initial time. k_1 is a spring parameter. k_2 is a damping parameter that can attenuate the oscillating behavior of the system. Δt is the time step. The appropriate values for these two parameters are heuristically chosen to ensure damped oscillator behavior. The values $k_1 = 1.9 \times 10^7\ \mathrm{s}^{-2}$ and $k_2 = 3 \times 10^3\ \mathrm{s}^{-1}$ have been selected and are used in all the simulations. For the present cases, these values minimize oscillations of the bubble center.

When bubbles are fixed, it is necessary to impose a new source term $\mathbf{S_2}$ in the r.h.s. of Eq. (8) to obtain the good relative velocity between phases (i.e., the good liquid flow rate). The expression $\partial\mathbf{S_2}/\partial t = -k_3\langle\mathbf{F}\rangle$ reaches a stationary state where $S_2^\infty = Cte$ while $\langle\mathbf{F}\rangle^\infty = 0$. Indeed, the dynamic equilibrium of bubbles is reached when the averaged drag force compensates for buoyancy. The source term $\mathbf{S_2}$ thus compensates the additional momentum induced by the work of $\mathbf{F}$ and the mean pressure gradient. In the code, it is calculated as

$$S_2^{n+1} = S_2^n - k_3\Delta t\,\langle\mathbf{F}\rangle^n; \quad S_2^0 = 0. \tag{13}$$

The coefficient $k_3 = 2 \times 10^4\ \mathrm{kg\,m^{-3}\,s^{-1}}$ is chosen to minimize flow-rate fluctuations.

III. TURBULENCE DECOMPOSITION

The purpose of this section is to explain the decomposition of the fluctuations in WIA and PWFs in the case of fixed bubbles and to adapt this decomposition to the Reynolds stresses transport equation.

A. WIA/PWF decomposition

Velocity fluctuations defined with the phase average ($\mathbf{u_l} = \mathbf{U_l} - \overline{\mathbf{U_l}}^{\mathbf{l}}$ with $\overline{\mathbf{U_l}}^{\mathbf{l}} = \overline{\chi_l\mathbf{U_l}}/\alpha_l$ and $\alpha_l = \overline{\chi_l}$) oscillate around zero in the interstitial region and the distribution of the fluctuations is symmetrical. Their behavior is chaotic as classical turbulence (WIA). On the other hand, in volumes located in the neighborhood of bubbles (mainly wakes), streamwise fluctuations are shifted towards positive values because of the liquid entrainment caused by bubbles. They are not turbulent but rather due to the velocity shift related to the bubble wake (PWFs).

By application of the ergodicity assumption, the statistical average $\overline{\phi}$ is split into a spatial average $\overline{\phi}^X$ and a time average $\overline{\phi}^T$ such that

$$\overline{\phi} = \overline{\overline{\phi}^X}^T = \overline{\overline{\phi}^T}^X. \tag{14}$$

Riboux and Legendre [8] have shown that in the reference frame of fixed bubbles, PWF and WIA contributions are easily separable and correspond, respectively, to the spatial fluctuations $\overline{\chi_l\mathbf{u_l}}^T(x)$ and to the temporal fluctuations $\chi_l\mathbf{u_l}'(x,t)$ by virtue of the classical mean/fluctuation properties:

$$\chi_l\mathbf{u_l}(x,t) = \overline{\chi_l\mathbf{u_l}}^T(x) + \chi_l\mathbf{u_l}'(x,t) \text{ with } \overline{\chi_l\mathbf{u_l}'}^T = 0, \tag{15}$$

$$\chi_l p_l(x,t) = \overline{\chi_l p_l}^T(x) + \chi_l p_l'(x,t) \text{ with } \overline{\chi_l p_l'}^T = 0. \tag{16}$$

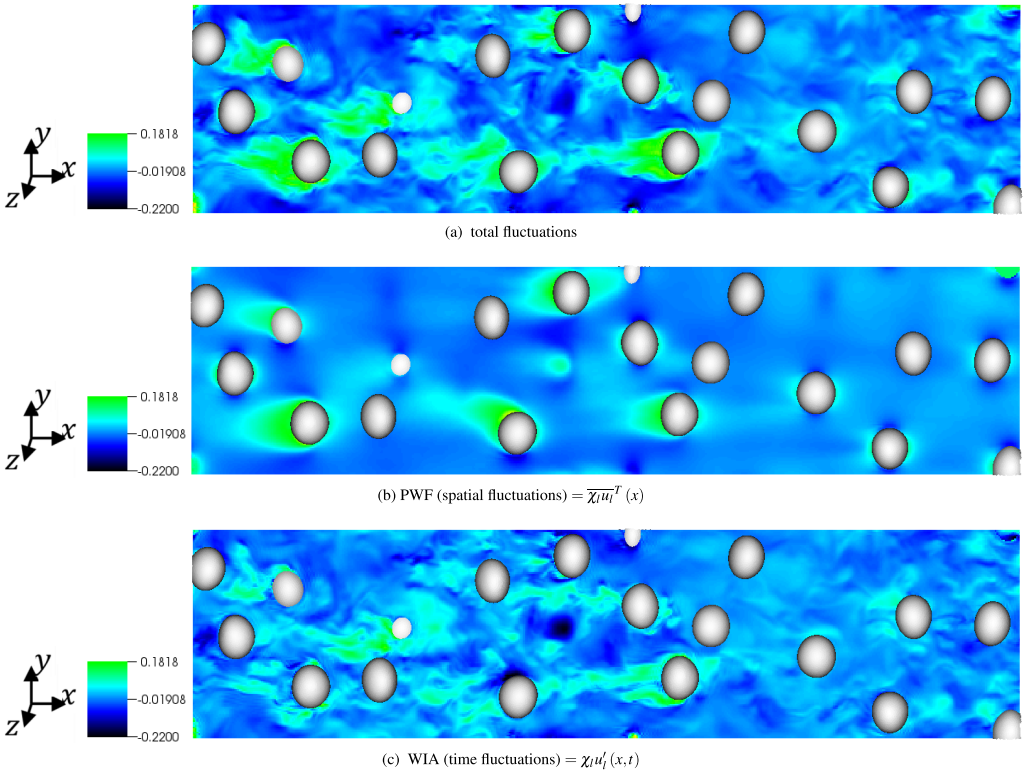

(a) total fluctuations

(b) PWF (spatial fluctuations) $= \overline{\chi_l u_l}^T(x)$

(c) WIA (time fluctuations) $= \chi_l u_l'(x,t)$

FIG. 3. Visualization of nonturbulent PWFs at $\mathrm{Re}_b = 438$ (b) [calculated as the time average of the instantaneous velocity field (a)] and turbulent WIA (c) = (a) − (b). Gravity follows the $-x$ axis.

This decomposition is illustrated in Fig. 3 from DNS results on a fixed bubbly flow. Second-order correlations are separated according to the previous expression. Let X_l and Y_l be two fields defined on the liquid phase, then

$$\overline{\chi_l X_l Y_l} = \overline{\overline{\chi_l X_l}^T \overline{\chi_l Y_l}^T}^X + \overline{\chi_l X_l' Y_l'} + \overline{\overline{\chi_l Y_l'}^T \overline{\chi_l X_l}^T}^X + \overline{\overline{\chi_l X_l'}^T \overline{\chi_l Y_l}^T}^X, \tag{17}$$

$$\overline{\chi_l X_l Y_l} = \overline{\overline{\chi_l X_l}^T \overline{\chi_l Y_l}^T}^X + \overline{\chi_l X_l' Y_l'}. \tag{18}$$

In particular, for $X_l = Y_l = \mathbf{u_l}$, Eq. (18) allows the decomposition of the Reynolds stress tensor into spatial fluctuations $\mathbf{R^{PWF}}$ and time fluctuations $\mathbf{R^{WIA}}$:

$$\underbrace{\overline{\chi_l \mathbf{u_l} \mathbf{u_l}}}_{\alpha_l \mathbf{R^{BIA}}} = \underbrace{\overline{\overline{\chi_l \mathbf{u_l}}^T \overline{\chi_l \mathbf{u_l}}^T}^X}_{\alpha_l \mathbf{R^{PWF}}} + \underbrace{\overline{\chi_l \mathbf{u_l}' \mathbf{u_l}'}}_{\alpha_l \mathbf{R^{WIA}}}. \tag{19}$$

It should be noted, however, that triple correlations do not decompose rigorously. In particular, the triple velocity correlation appearing in the turbulent diffusion term of the Reynolds stress transport equation reveals a third term that does not cancel out. It is an interaction term between WIA and PWFs:

$$\overline{\chi_l \mathbf{u_l} \mathbf{u_l} \mathbf{u_l}} = \underbrace{\overline{\overline{\chi_l \mathbf{u_l}}^T \overline{\chi_l \mathbf{u_l}}^T \overline{\chi_l \mathbf{u_l}}^T}^X}_{PWF} + \underbrace{\overline{\chi_l \mathbf{u_l}' \mathbf{u_l}' \mathbf{u_l}'}}_{WIA} + \underbrace{3\overline{\overline{\chi_l \mathbf{u_l}}^T \overline{\chi_l \mathbf{u_l}' \mathbf{u_l}'}^T}^X}_{PWF/WIA \neq 0}. \tag{20}$$

B. Decomposition of the Reynolds stress transport equation

Following the process described by Morel [21], we obtain the transport equation of velocity fluctuations, and then the transport equation of Reynolds stresses:

$$\frac{D\alpha_l \overline{u_{l,i}u_{l,j}}^l}{Dt} + \underbrace{\alpha_l \overline{u_{l,i}u_{l,b}}^l \frac{\partial U_{l,j}}{\partial x_b} + \alpha_l \overline{u_{l,j}u_{l,b}}^l \frac{\partial U_{l,i}}{\partial x_b}}_{-P_{ij}} \tag{21}$$

$$= \underbrace{\alpha_l \overline{\frac{p_l}{\rho_l}\left(\frac{\partial u_{l,i}}{\partial x_j} + \frac{\partial u_{l,j}}{\partial x_i}\right)}^l}_{\phi_{ij}} \underbrace{-2\,\alpha_l \frac{\mu_l}{\rho_l} \overline{\frac{\partial u_{l,i}}{\partial x_b}\frac{\partial u_{l,j}}{\partial x_b}}^l}_{\epsilon_{ij}}$$

$$\underbrace{-\frac{\partial}{\partial x_b}\left(\alpha_l \overline{u_{l,i}u_{l,j}u_{l,b}}^l - \nu_l \frac{\partial \alpha_l \overline{u_{l,i}u_{l,j}}^l}{\partial x_b} + \frac{\alpha_l}{\rho_l}\left(\overline{p_l u_{l,i}}^l \delta_{bj} + \overline{p_l u_{l,b}}^l \delta_{ib}\right)\right)}_{D_{ij}}$$

$$\underbrace{-\frac{1}{\rho_l}\overline{(p_l u_{l,j} n_i + p_l u_{l,i} n_j)\delta^i}^l + \nu_l \left[\frac{\partial}{\partial x_b}\left(\overline{u_{l,i}u_{l,j}n_j\delta^i}^l\right) + \overline{\frac{\partial u_{l,i}u_{l,j}}{\partial x_b}n_b\delta^i}^l\right]}_{\Pi_{ij}},$$

where D/Dt is the material derivative.

Using the correlation decomposition (18) on Eq. (21), we can separate each statistical averaged term into space and time averaged terms. If bubbles are fixed, space, and time averages are independent and coincide with WIA and PWFs, respectively. Only the terms Π_{ij} and a part of D_{ij} (turbulent diffusion) cannot be separated this way.

For the decomposition of the interfacial production Π_{ij}, we define Π_{ij}^{PWF} as the interfacial production related to spatial inhomogeneities and Π_{ij}^{WIA} as the turbulent production due to wake interaction:

$$\Pi_{ij}^{PWF} + \Pi_{ij}^{WIA} = \Pi_{ij}. \tag{22}$$

Definitions of Π_{ij}^{PWF} and Π_{ij}^{WIA} possibly could be given by introducing new averages on the interfaces. In this work, they are not directly measured.

Lastly, for the turbulent diffusion, we assume that the interaction between PWFs and WIA related to the decomposition of the triple correlation [Eq. (20)] is negligible:

$$\overline{\chi_l \mathbf{u_l}\mathbf{u_l}\mathbf{u_l}} \gg 3\overline{\overline{\chi_l \mathbf{u_l}}^T \overline{\chi_l \mathbf{u_l'}}^T}^X. \tag{23}$$

Finally, the aim is to separate the Reynolds stress transport equation in two: an equation with spatial averages (PWFs), and one with time averages (WIA). However, strong nonlinear interactions occur between WIA and PWFs and must be taken into account in those equations. To be exhaustive, we must add an unknown energy transfer term from WIA to PWFs (T_{ij}) to each equation [note that the neglected part of the triple correlation in Eq. (23) can be seen as a part of this transfer term]. Thus, we obtain the following two equations:

1. Transport equation for space fluctuations $\alpha_l R_{ij}^{PWF} = \overline{\overline{\chi_l u_{l,i}}^T \overline{\chi_l u_{l,j}}^T}^X$

$$
\begin{aligned}
&\frac{D\alpha_l R_{ij}^{PWF}}{Dt} + \alpha_l R_{ib}^{PWF}\frac{\partial U_{l,j}}{\partial x_b} + \alpha_l R_{jb}^{PWF}\frac{\partial U_{l,i}}{\partial x_b} \\
&= \overline{\frac{\chi_l p_l}{\rho_l}^T \left(\chi_l \frac{\partial u_{l,i}}{\partial x_j}^T + \chi_l \frac{\partial u_{l,j}}{\partial x_i}^T\right)}^X - 2\frac{\mu_l}{\rho_l}\overline{\chi_l \frac{\partial u_{l,i}}{\partial x_b}^T \chi_l \frac{\partial u_{l,j}}{\partial x_b}^T}^X \\
&- \frac{\partial}{\partial x_b}\left(\overline{\overline{\chi_l u_{l,i}}^T \overline{\chi_l u_{l,j}}^T \overline{\chi_l u_{l,b}}^T}^X - \nu_l \frac{\partial \alpha_l R_{ij}^{PWF}}{\partial x_b}\right) \\
&- \frac{\partial}{\partial x_b}\left(\frac{1}{\rho_l}\left(\overline{\overline{\chi_l p_l}^T \overline{\chi_l u_{l,i}}^T}^X \delta_{bj} + \overline{\overline{\chi_l p_l}^T \overline{\chi_l u_{l,b}}^T}^X \delta_{ib}\right)\right) \\
&+ \Pi_{ij}^{PWF} + T_{ij}.
\end{aligned}
\tag{24}
$$

This equation can be used as a support for PWF modeling as in Ref. [13]. It can be reduced to the following form:

$$
\begin{aligned}
\frac{D\alpha_l R_{ij}^{PWF}}{Dt} &= P_{ij}^{PWF} + \phi_{ij}^{PWF} - 2\epsilon_{ij}^{PWF} \\
&\quad + D_{ij}^{PWF} + \Pi_{ij}^{PWF} + T_{ij}.
\end{aligned}
\tag{25}
$$

P_{ij}^{PWF}, ϕ_{ij}^{PWF}, ϵ_{ij}^{PWF}, and D_{ij}^{PWF} are directly measured from DNS results and $\Pi_{ij}^{PWF} + T_{ij}$ is calculated as the residue of the equation (see [13] for another use of this method). As previously mentioned, in the future we may consider giving a definition to the interfacial production to separate production from transfer. In this work however, a joint modeling of production and transfer terms is sufficient, as will be illustrated in the following sections.

2. Transport equation for time fluctuations $\alpha_l R_{ij}^{WIA} = \overline{\chi_l u'_{l,i} u'_{l,j}}$

$$
\begin{aligned}
&\frac{D\alpha_l R_{ij}^{WIA}}{Dt} + \alpha_l R_{ib}^{WIA}\frac{\partial U_{l,j}}{\partial x_b} + \alpha_l R_{jb}^{WIA}\frac{\partial U_{l,i}}{\partial x_b} \\
&= \overline{\frac{\chi_l p'_l}{\rho_l}\left(\frac{\partial u'_{l,i}}{\partial x_j} + \frac{\partial u'_{l,j}}{\partial x_i}\right)} - 2\frac{\mu_l}{\rho_l}\overline{\chi_l \frac{\partial u'_{l,i}}{\partial x_b}\frac{\partial u'_{l,j}}{\partial x_b}} \\
&- \frac{\partial}{\partial x_b}\left(\overline{\chi_l u'_{l,i} u'_{l,j} u'_{l,b}} - \nu_l \frac{\partial \alpha_l R_{ij}^{WIA}}{\partial x_b}\right) \\
&- \frac{\partial}{\partial x_b}\left(\frac{1}{\rho_l}\left(\overline{\chi_l p'_l u'_{l,i}}\delta_{bj} + \overline{\chi_l p'_l u'_{l,b}}\delta_{ib}\right)\right) \\
&+ \Pi_{ij}^{WIA} - T_{ij}.
\end{aligned}
\tag{26}
$$

Note that in this expression, u' and p' are temporal fluctuations as defined in Eqs. (15) and (16). This expression reduces to

$$
\begin{aligned}
\frac{D\alpha_l R_{ij}^{WIA}}{Dt} &= P_{ij}^{WIA} + \phi_{ij}^{WIA} - 2\epsilon_{ij}^{WIA} \\
&\quad + D_{ij}^{WIA} + \Pi_{ij}^{WIA} - T_{ij},
\end{aligned}
\tag{27}
$$

where P_{ij}^{WIA}, ϕ_{ij}^{WIA}, ϵ_{ij}^{WIA}, D_{ij}^{WIA} are directly measured via DNS results and $\Pi_{ij}^{WIA} - T_{ij}$ is calculated as the residue of the equation.

Thus formed, the two equations (25) and (27) amount to an alternative formulation of the total Reynolds stress transport equation. In the case of a fixed bubbles, these equations can be used to study WIA and PWFs separately from DNS results, and can be used as a support for the modeling of the transport equation. This is the purpose of the following sections.

IV. PHYSICAL ANALYSIS OF HOMOGENEOUS BUBBLY FLOWS

The purpose of this section is to describe the main physical mechanisms of a bubbly flow (Sec. IV A) and to study differences between free-bubble and fixed-bubble configurations (Sec. IV B). The last section IV C is devoted to the study of PWF and WIA characteristics.

A. General remarks

The instantaneous fields in Figs. 4(a) and 4(b) provide crucial information on the dynamics of bubbles. As the Reynolds number increases, more turbulent structures and smaller vortices appear. This observation is valid for both fixed- and free-bubble simulations.

The formation of bubble clusters is observed in the case of free bubbles [Fig. 4(b)]. The clusters occur at low bubble Reynolds numbers and become less apparent when the Reynolds number is increased. This attenuation can be interpreted as an increase of the turbulent dispersion effect, which mixes more effectively the entire flow. At low Reynolds numbers, bubbles form clusters in horizontal rafts. This is a phenomenon related to pressure effects generated by the potential flow around spherical bubbles. In experiments, such alignments are rarely observed because bubbles do not remain sufficiently spherical. There are many shocks between bubbles (bouncing) which cause a very significant slowdown of bubbles located in the cluster. In addition to bouncing and interactions, purely hydrodynamical effects decrease the bubble velocity as the cross section for counterflow decreases. The "local" void fraction clearly influences the average velocity of bubbles. Here the average void fraction "seen by the bubble" (in the cluster) is high (roughly above 10%), and we observe a decrease of the relative velocity compared to a random distribution of fixed bubbles which "see" an average void fraction of 6% (see Fig. 5). These local variations of void fraction can cause large differences in statistical results, not just in relative velocities. For example, wakes of bubbles located in a cluster have no space to develop and a significant decrease in s is therefore expected (see Fig. 5). By decreasing the relative velocity of bubbles, the production of WIA is also decreased.

Another phenomenon is particularly visible by comparing Figs. 4(a) and 4(b) at their respectively lowest Reynolds number. In the case of fixed bubbles, vortical structures in the wakes are long and vertically aligned. Observing their time evolution, one realizes that they are almost stationary (namely, comprising PWFs exclusively). The wake lengths can then reach 3 or 4 times the bubble diameter. In the case of free bubbles, this behavior disappears in favor of a much more disordered flow. Structures are no longer stationary and are much shorter than in the case of fixed bubbles (PWFs much smaller and emergence of WIA), this collective destabilization effect is probably due to the relative motion of bubbles as it is lacking in the simulations with fixed bubbles. When bubbles move and cross the wakes of their neighbors, with velocities relative to each other, they destabilize the flow for Reynolds numbers lower than in the case of fixed bubbles. At low Reynolds number, we observe different distributions of WIA/PWFs depending on the case considered (free or fixed). Moreover, it is probable that this effect remains for higher Reynolds numbers but it is then more difficult to observe from instantaneous fields. Thus, the features observed in fixed-bubble simulations are affected by the lack of relative bubble motion.

Most of the preceding observations are confirmed in Fig. 5 where the relative velocity and the Reynolds stresses are compared between fixed- and free-bubble configurations. The relative velocity is almost constant for all free-bubble simulations with a slight increase with the Reynolds number. This effect can be related to both an increase in the homogeneity of the bubble distribution with

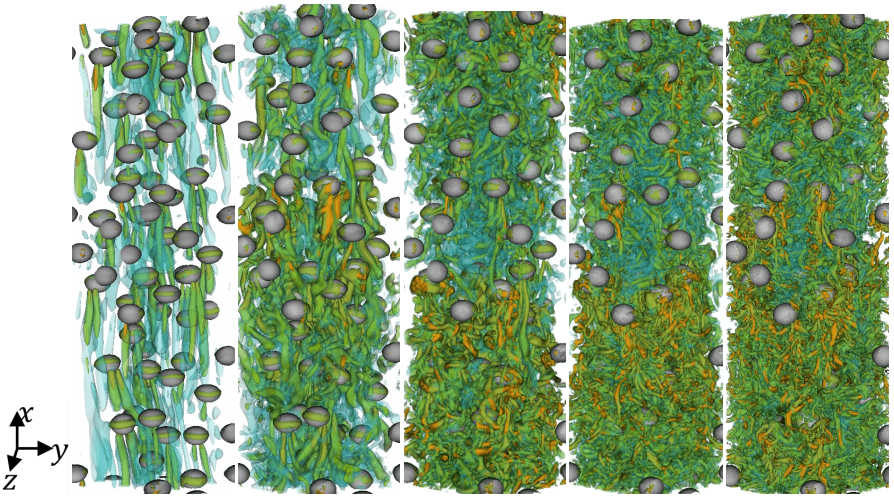

(a) Fixed bubbles: $Re_b = 118$, 229, 438, 630 and 786 from left to right

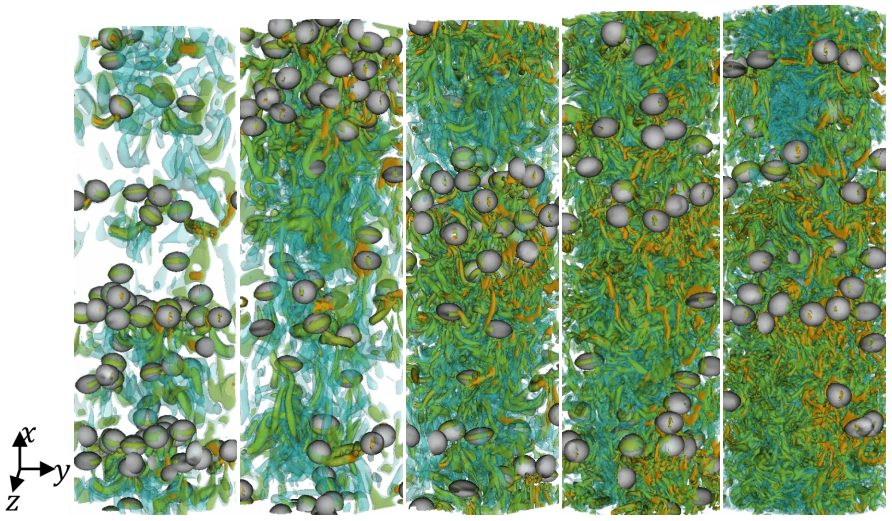

(b) Free bubbles: $Re_b = 72$, 171, 345, 539 and 684 from left to right

FIG. 4. Instantaneous representations of bubbly flows for fixed (a) and free (b) bubbles. The vortical structures are isovalues of the λ_2 criterion with different intensities (weak in blue, medium in green, strong in orange) [66]. See [67] for additional elements on the simulations.

the Reynolds number (as observed on the instantaneous fields) and a decrease of the viscosity. For $\mathrm{Re}_b \to \infty$, we can assume that the two curves (fixed and free) would meet if the distribution of free bubbles became homogeneous. For fixed bubbles, the relative velocity is higher, reflecting the impact of their distribution; bubbles are much more interacting in free cases. The relative velocity obtained for fixed-bubble cases decreases with the Reynolds number. It can be assumed that this result is due to a transfer from the mean kinetic energy of bubbles towards the turbulent kinetic energy of the liquid. Thus, differences between the relative velocities of fixed and free bubbles seem mainly due to the spatial distribution of bubbles. Concerning the Reynolds stresses, nondiagonal components are zero in the absence of a wall. A similar behavior between fixed and free bubbles on transversal components is observed (R_{22} and R_{33}). Note that the perfect equality between components R_{22} and R_{33} reflects a very good convergence of statistics. On these components, PWFs

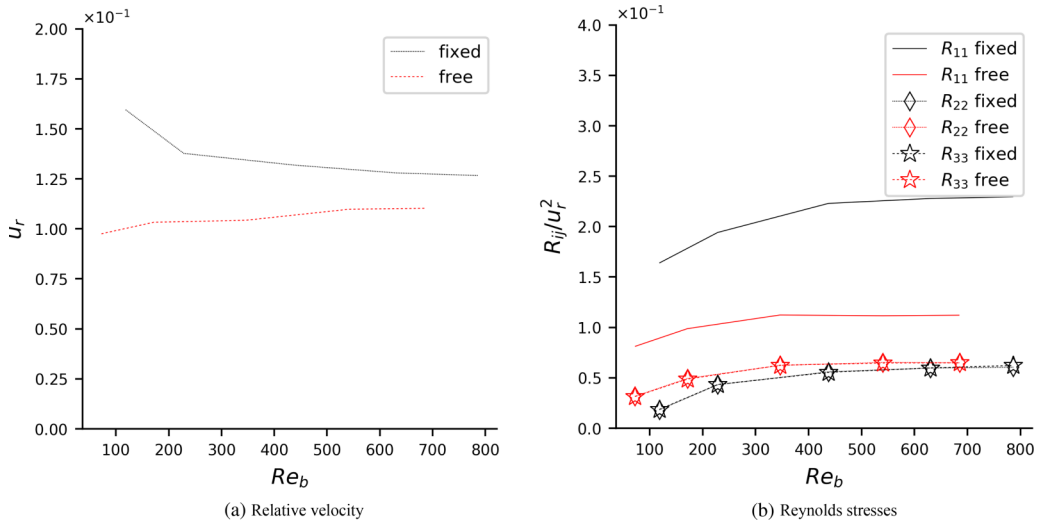

(a) Relative velocity (b) Reynolds stresses

FIG. 5. Relative velocity (a) and normalized Reynolds stresses (b) vs bubble Reynolds number for fixed-bubble and free-bubble configurations.

are weak. This result suggests that WIA does not vary widely between the two configurations in transversal directions. The present data leads us to think that WIA characteristics in the streamwise direction are also conserved. This equivalence in WIA between the two configurations is an essential result because the main interest of these simulations lies in their use for the construction of WIA model. On the other hand, on the streamwise component, the total Reynolds stresses are twice bigger in the case of fixed bubbles. PWFs in the case of fixed bubbles are much greater because of a more homogeneous distribution of bubbles and of the absence of turbulent motions of bubbles which favor the establishment of large wakes. Despite these differences, PWFs evolve similarly for fixed and free bubbles.

B. Differences between free- and fixed-bubble flows

In the collective bubble frame and at equilibrium, the drag force and the buoyancy are balanced and the control force on bubbles oscillates around zero to prevent the relative motion of bubbles. Two effects can therefore explain the differences observed between fixed-bubble and free-bubble calculations:

(1) The impact of the spatial distribution of bubbles

(2) The impact of the relative motion of bubbles (linked to the power of the control force).

In order to better understand the respective effects of these two phenomena, a fixed-bubble calculation was carried out with an inhomogeneous distribution of bubbles taken from a snapshot of a free calculation.

After reaching the stationary state, the interfaces of the free case at $\mathrm{Re}_b \approx 400$ have been extracted to be used as an initial condition in a fixed-bubble calculation. Table III relates the main results of this study. Overall, we observe a better prediction of all the variables in the case of inhomogeneously distributed bubbles. In particular, the error on the relative velocity falls from 26% to 12%. The decrease in velocity is explained by the influence of the local void fraction as stated in the previous section. The error on transverse Reynolds stresses decreases dramatically from 13%–20% to 1%. This result is encouraging in the prospect of studying WIA. Indeed, in transverse directions, fluctuations are mainly composed of WIA, and this result shows that fixing bubbles do not alter the evaluation of the WIA in these directions. Assuming that WIA is almost isotropic (see Sec. V C), we can infer that the same occurs in the streamwise direction. Modeling of WIA could

TABLE III. Average quantities in the case of fixed bubbles (with homogeneous or inhomogeneous bubble repartition) and free bubbles at $\mathrm{Re}_b \approx 400$. The case with free bubbles is the reference for the calculation of the relative error.

	Free bubbles (Ref.)	Fixed bubbles			
		Homogeneous		Inhomogeneous	
		Value	Relative error	Value	Relative error
u_r [m/s]	0.105	0.132	26%	0.118	12%
R_{11} [m^2/s^2]	0.00125	0.0036	188%	0.0031	148%
R_{22} [m^2/s^2]	0.00075	0.0009	20%	0.000756	1%
R_{33} [m^2/s^2]	0.000749	0.00085	13%	0.00075	0%
Π_{11} [m^2/s^3]	0.075	0.135	80%	0.105	40%

be improved in further studies by running fixed-bubbles simulations with inhomogeneous spatial distributions, taken from steady-state snapshots of free-bubble simulations.

The error on Reynolds stresses in the streamwise direction is important in both situations (between 150% and 190% error). In this direction, at a given relative velocity, fluctuations are mainly related to the size of the averaged wakes. Thus, fixing a bubble increases the size of its wake (and its relative velocity) regardless of the bubble distribution. We observe that this increase is concomitant with an increase of the interfacial production term Π (see also Fig. 7). Then, the error on Π is important as well. This overproduction of energy is revealed via the increase of the length of the wakes (namely, of PWFs). Thus, the study of PWFs via a fixed-bubble calculation is compromised since the wake size is strongly influenced by the bubble artificial force. A PWF model based on such results would not have strong physical basis. However, no energy transfer from the exceeding PWF to the WIA is observable; the exceeding energy due to the control force is completely dissipated in the wakes without creating more turbulent fluctuations. So WIA does not seem unduly impacted by the bubble artificial force. Therefore, the data on fixed bubbles can be exploited for the purpose of WIA modeling. Then PWFs can be deduced from free-bubble simulations by subtracting the contribution of the modeled WIA from the total fluctuations. Final verification of the model as a whole is performed in Sec. V E.

C. Properties of turbulence

In this section, statistical methods are used to check the main characteristics of bubble-induced turbulence. The probability density functions (PDFs) of the velocity fluctuations are estimated using histograms based on the values of the velocity field in each cell of the domain, recorded over several independent time steps of the statistical equilibrium. In the case of fixed bubbles, we are able to separate PWF and WIA contributions (see Sec. III) and thereby PDFs corresponding to each part can be plotted independently. In the case of free bubbles, only PDFs of total fluctuations can be plotted. These results are gathered in Fig. 6. For both cases, PDFs of total fluctuations show that the distribution of fluctuations is not symmetrical. The shift towards positive values is due to the averaged wakes (PWFs) [16]. The shift is more pronounced for fixed bubbles. This result is consistent with the fact that fixed bubbles generate more PWFs than free bubbles. We also find that PDFs of total fluctuations have exponentially decreasing tails as in the experimental work [8]. Once normalized by the variance, it is observed that PDFs of total fluctuations are relatively independent of the Reynolds number (between 100 and 1000).

Once the fluctuations are divided into PWFs and WIA (for fixed bubbles), we notice that the majority of the shift towards positive values is due to the PWF. Part of this shift is also found in the WIA. We have previously shown that WIA consists of two phenomena: the collection of nonstationary wakes which is not necessarily turbulent and the collective wake instability which is a turbulent phenomenon. The collective instability of wakes appears only for large Reynolds

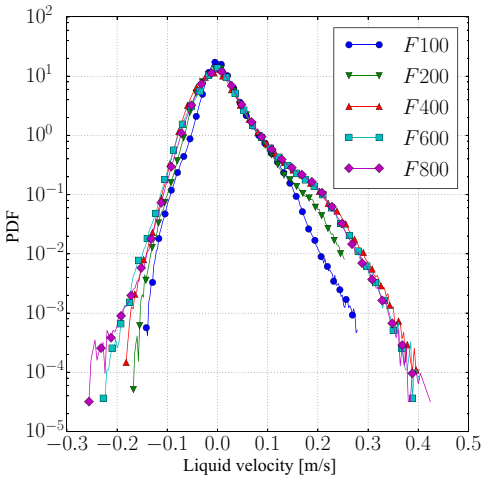

(a) pdfs of total fluctuations (fixed bubbles)

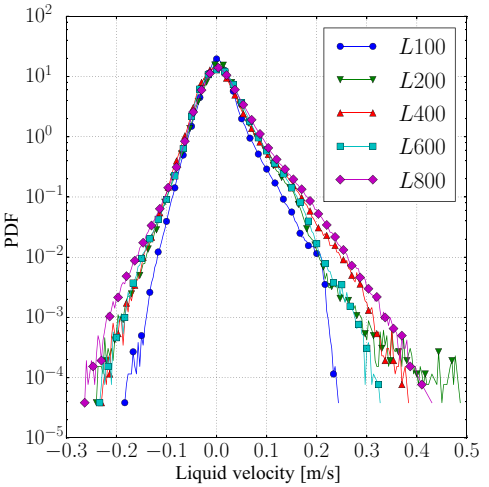

(b) pdfs of total fluctuations (free bubbles)

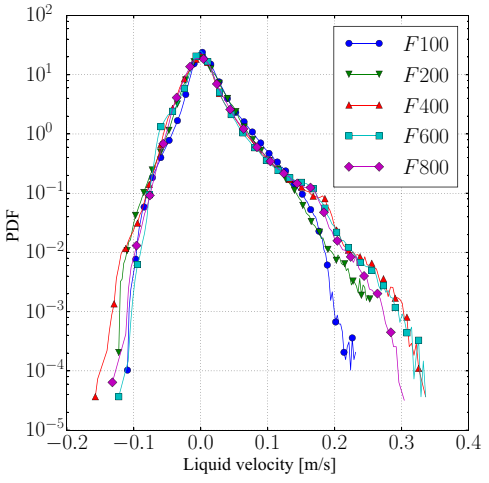

(c) PWF pdfs (fixed bubbles)

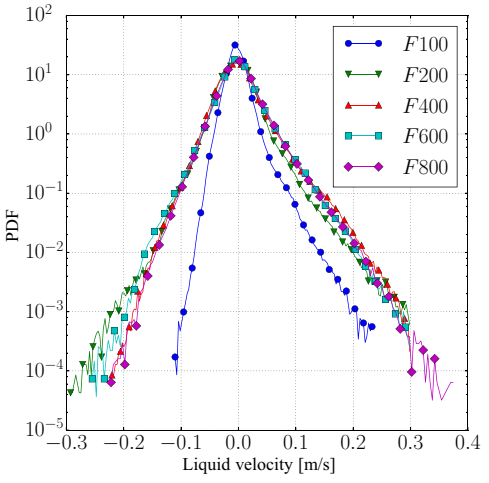

(d) WIA pdfs (fixed bubbles)

FIG. 6. Normalized PDFs of streamwise velocity fluctuations for fixed (a) and free bubbles (b) and decomposition of PDFs into PWF (c) and WIA (d) for fixed bubbles. See Table IV for the normalization constants. For the case nomenclature: F = fixed, L = free. The letter is followed by the bubble Reynolds number.

numbers (see Ref. [17]). In the case F100 at $\mathrm{Re}_b = 100$, WIA is therefore a simple collection of nonstationary wakes. It can be seen in Fig. 6(d) that, in this case, the PDF is not symmetric at all. We can then assume that the part of asymmetry in WIA PDFs is related to the wakes. Thus, the collective instability appearing when the Reynolds number is increased is in fact a symmetric PDF, in accordance with a classical turbulent phenomenon. The asymmetric part of the WIA appears important in the F100 case because of the normalization of the PDFs, yet it contains only 6.8% of the total energy (see Table IV). For all the other Reynolds numbers, WIA PDFs are fairly symmetrical, and almost all the shift towards positive values is absorbed by PWF PDFs in Fig. 6(c). At first order, we can therefore consider that WIA has a symmetric distribution.

Guaranteeing the properties of bubble-induced turbulence in the case of fixed bubbles, these results ensure the quality of the simulations.

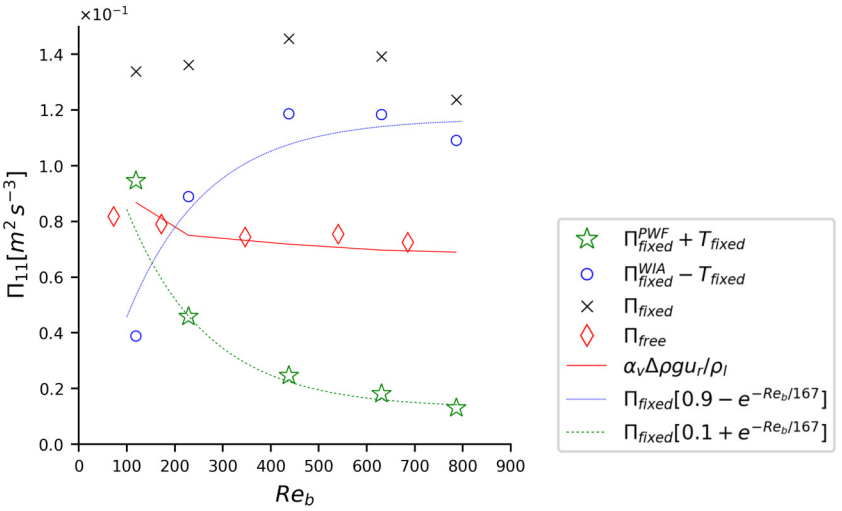

FIG. 7. Interfacial production term as a function of the bubble Reynolds number for fixed and free bubbles. For fixed bubbles, decomposition in WIA and PWF production.

V. BUBBLE-INDUCED AGITATION MODEL FOR BUBBLY FLOWS

Due to the homogeneity assumption, we have: $\partial\overline{\phi}^{l}/\partial x_i = \partial\overline{\phi}^{T}/\partial x_i = \partial\overline{\phi}^{X}/\partial x_i = 0\ \forall i$, which simplifies the WIA transport equation (27). Besides, at the stationary state, it simplifies to a balance between redistribution, dissipation, interfacial production, and transfer from WIA to PWF:

$$\phi_{ij}^{WIA} - 2\epsilon_{ij}^{WIA} + \Pi_{ij}^{WIA} - T_{ij} = 0. \tag{28}$$

The purpose of this section is to study each of these terms in order to propose a model for WIA fluctuations. In the case of fixed-bubble calculations, each of these terms is given by its definition in Eq. (26). Thus, this section presents a model for the WIA based on its transport equation. We know from Sec. IV that fixing bubbles significantly alter the estimation of PWFs. The calibration of an existing PWF model is therefore based on free-bubble calculations (see Sec. V E). Finally, a complete model of bubble-induced turbulence is proposed at the end of this section.

A. WIA interfacial production and transfer

As seen in Sec. III, the interfacial production and the energy transfer between WIA and PWFs cannot be separated in this study. We will therefore try to interpret and model them together.

Classically, the total interfacial production (PWF + WIA) is assimilated to the power of the drag force [21]. It is then assumed that the power of other interfacial forces (lift, turbulent dispersion, etc.) is negligible compared to that of the drag force. At first order, we consider $\Pi_{ij} = \Pi_{11}\delta_{i1}\delta_{j1}$.

TABLE IV. PDF normalization for streamwise velocity fluctuations. The coefficients for R_{11}^{PWF} and R_{11}^{WIA} are expressed as a percentage of the total streamwise velocity fluctuation R_{11}^{tot}.

	L100	L200	L400	L600	L800	F100	F200	F400	F600	F800
R_{11}^{tot} [$\times 10^{-3}$ m^2 s^{-2}]	0.77	1.05	1.22	1.34	1.36	4.16	3.68	3.87	3.73	3.67
R_{11}^{PWF} [%]						93.2	88.7	77.7	76.2	73
R_{11}^{WIA} [%]						6.8	11.3	22.3	23.8	27

This hypothesis is corroborated by DNS results and extended to transfer between PWFs and WIA. Indeed, among the components of the tensor $\Pi_{ij}^{WIA} - T_{ij}$, the component (1, 1) (corresponding to the streamwise direction) is predominant before the transverse components. Then

$$\Pi_{ij}^{WIA} - T_{ij} = \left(\Pi_{11}^{WIA} - T_{11}\right)\delta_{i1}\delta_{j1}, \tag{29}$$

$$\Pi_{ij}^{PWF} + T_{ij} = \left(\Pi_{11}^{PWF} + T_{11}\right)\delta_{i1}\delta_{j1.} \tag{30}$$

In Fig. 7, the sum of production and transfer (total, WIA, and PWF) is plotted for fixed bubbles along with the total production for free bubbles. A difference is observed between the total production of free bubbles and that of fixed bubbles. The origin of this difference has been discussed in Sec. IV B. Figure 7 shows that the production in the case of free bubbles is in good agreement with the power of the drag force given by $\alpha_v \frac{\Delta\rho}{\rho_l} g u_r$. Note that fixing bubbles make the correlation obsolete due to the influence of the control force.

In the case of fixed bubbles, the interaction between PWF and WIA is interesting. Physically, at low Reynolds number, bubble wakes are stable and produce PWFs exclusively. With the increase of the Reynolds number, wakes are destabilized and their interactions lead to the creation of WIA. This conversion from PWF to WIA is characterized in Fig. 7 by the decrease of the sum of PWF production and transfer $\Pi_{\text{fixed}}^{PWF} + T$ with increasing Reynolds number and by the concurrent increase of WIA production and transfer. These two variations compensate one another, in agreement with a total interfacial production independent of the Reynolds number, as expressed by the correlation for the power of the drag force. Finally, the total production remains relatively constant. This behavior is the signature of an energy conversion from wake kinetic energy (PWF) to turbulent kinetic energy (WIA) and shows the importance of nonlinear interactions and transfers between PWF and WIA. The phenomenon of wake destabilization involves strongly nonlinear interactions that are difficult to describe formally. Then we propose to describe these interactions with an empirical method. Based on our results, we write

$$\Pi_{\text{fixed}}^{WIA} - T = \Pi_{\text{fixed}}\left(0.9 - e^{-\frac{\text{Re}_b}{\text{Re}_b^c}}\right), \tag{31}$$

$$\Pi_{\text{fixed}}^{PWF} + T = \Pi_{\text{fixed}}\left(0.1 + e^{-\frac{\text{Re}_b}{\text{Re}_b^c}}\right), \tag{32}$$

where the critical Reynolds number $\text{Re}_b^c = 170$ characterizes the emergence of the collective wake instability responsible for the appearance of WIA. The value of 170 is also in agreement with the instabilities observed experimentally in Refs. [8,17]. As described in Ref. [17], we notice an asymptotic convergence of the production for the higher Reynolds numbers. For $\text{Re}_b \to \infty$, the PWF does not completely disappear (as some wakes remain, and the potential flow as well). The asymptotic value of PWF scan be assessed from the DNS results as $0.1\Pi_{\text{fixed}}$ while the asymptotic value of WIA tends to $0.9\Pi_{\text{fixed}}$ for $\text{Re}_b \to \infty$. This asymptotic behavior explains the form of the empirical closure given in Eqs. (31) and (32). However, the values 0.1, 0.9, and Re_b^c have to be further confirmed by experimental results.

Assuming that the repartition between PWF and WIA does not depend on the total production, we extrapolate this closure to any production that verifies $\Pi = \alpha_v \Delta\rho g u_r/\rho_l$. Thus, the final model for WIA production and transfer is

$$\Pi_{ij}^{WIA} - T_{ij} = \alpha_v \frac{\Delta\rho}{\rho_l} g u_r \left(0.9 - e^{-\frac{\text{Re}_b}{\text{Re}_b^c}}\right)\delta_{i1}\delta_{j1}. \tag{33}$$

This relation provides a closure to the two last terms of Eq. (28). The following section addresses the modeling of the dissipation.

B. WIA dissipation

In this part, we summarize various works which have led to the proposal of a scaling law for the WIA dissipation by Risso [7]. This law is then tested on our DNS results.

Let us follow the approach of Lance and Bataille [1] to write the Navier-Stokes equations in Fourier space. Let E be the turbulent energy density, T the energy transfer between frequencies, and Π the interfacial production. Then the Fourier transform of the kinetic energy transport equation reads

$$\frac{\partial E}{\partial t} + 2\nu\kappa^2 E = T + \Pi, \tag{34}$$

where κ is the wave number. Considering that the production Π has a short range of wavelength (bubbles inject their energy at a particular frequency close to the bubble size), Lance and Bataille [1] show by dimensional analysis that

$$\Pi \propto \kappa^{-1}\epsilon. \tag{35}$$

This leads to the following statistical equilibrium:

$$E \propto \frac{\epsilon\kappa^{-3}}{2\nu}. \tag{36}$$

This scaling of the turbulent energy spectrum ($\propto \kappa^{-3}$) has been extensively verified, both numerically and experimentally [8,69]. Once normalized by the variance, Riboux [70] shows empirically with experimental data that the kinetic energy spectrum is independent of the void fraction such that

$$\frac{E}{\langle uu\rangle\Lambda} \propto (\Lambda\kappa)^{-3}. \tag{37}$$

Therefore, the integral length scale Λ of bubble-induced turbulence can not be characterized by a mean distance between bubbles. We can note that Eqs. (36) and (37) are equivalent to

$$\epsilon \propto \frac{\nu\langle uu\rangle}{\Lambda^2}. \tag{38}$$

We find here a classical scaling law for single-phase flows, linking the dissipation rate to the variance of velocity fluctuations with a Taylor scale. The Taylor scale is here replaced by the integral length scale Λ. Reference [7] proposes a verification of this law by using the relation obtained experimentally for the variance [70]

$$\langle uu\rangle \propto \alpha_v^{0.8}\langle u_r\rangle^2 \approx \alpha_v\langle u_r\rangle^2, \tag{39}$$

a scaling law of the dissipation rate

$$\epsilon = \alpha_v g\langle u_r\rangle, \tag{40}$$

and the equilibrium between gravity and drag force at steady state

$$g \propto \frac{C_d\langle u_r\rangle^2}{d_b}. \tag{41}$$

Using the definition of the bubble Reynolds number ($\mathrm{Re}_b = \langle u_r\rangle d_b/\nu$) and Eqs. (38) to (41), the integral length scale should verify the following laws:

$$\Lambda \propto \sqrt{\frac{\nu\langle uu\rangle}{\epsilon}} \propto \frac{d_b}{\sqrt{C_d\mathrm{Re}_b}}. \tag{42}$$

Riboux [70] observes that the integral length scale behind a bubble swarm (i.e., in the absence of PWFs) is proportional to the bubble diameter and to the inverse of the drag coefficient: $\Lambda \propto d_b/C_d$. The expression (42) is in agreement with this result because $d_b/\sqrt{C_d\mathrm{Re}_b}$ is proportional to d_b/C_d

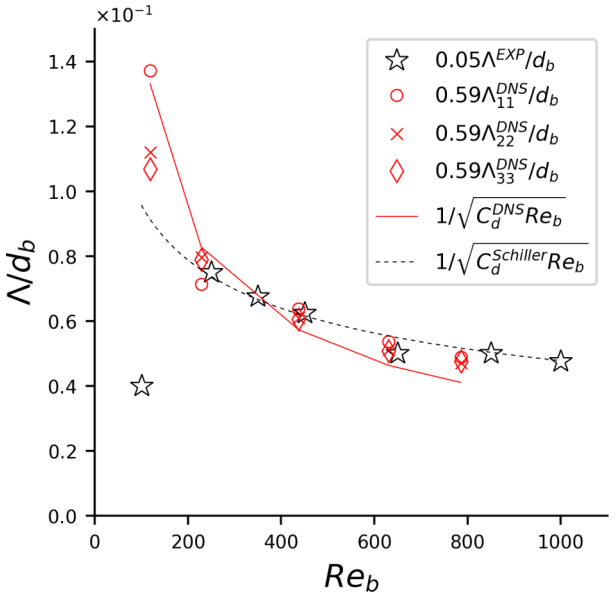

FIG. 8. Integral length scale as a function of the bubble Reynolds number. Markers: measurement of the integral length scale from the experimental autocorrelation signal (black stars) [17] or from the dissipation rate and Reynolds stresses from the DNS (red). Line: scaling laws involving a drag coefficient calculated from the DNS as $C_d = \frac{4}{3}\frac{\alpha_v d_b(\rho_l-\rho_v)g}{\rho_l u_r^2}$ (continuous red) or via the correlation of Schiller and Naumann [68] $C_d = \frac{24}{\mathrm{Re}_b}(1+0.15\mathrm{Re}_b^{0.687})$ (dashed black).

noting that $\mathrm{Re}_b \propto C_d$ [70]. The expression (42) has been obtained behind a swarm. This zone does not contain any wakes, and only their collective instability remains (no PWFs or nonstationary wakes); its validity inside the swarm itself has to be demonstrated. Reference [7] compares the experimental results of Ref. [17] obtained on an array of fixed spheres to this theory (this result is reported in black in Fig. 8). The scaling law (42) matches their experimental results for a wide range of bubble Reynolds numbers, even though for the lowest Reynolds number ($\mathrm{Re}_b \approx 150$) a sudden change is observed. This change can be explained by the fact that WIA then contains the nonstationary part of the wakes (contrary to the observation behind a bubble swarm). At low Reynolds number, collective instability tends to disappear and the nonstationary part of the wakes becomes the principal contribution of the WIA; for this reason, the trend can change because the integral length scale represents a different phenomenon (a wake collection instead of a collective instability). Thus, the scaling law (42) seems adequate for WIA modeling when the contribution of nonstationary wakes is negligible in comparison with their collective instability. We propose to check this assumption via our DNS calculations.

Direct measurement of the integral length scale from the autocorrelation signal (method used in Ref. [17]) leads to significant errors in the case of our DNS. The dissipation rate of the WIA can be directly assessed through the decomposition presented in Sec. III.

Therefore, we want to verify, for each diagonal component of the Reynolds stress tensor separately, the following relation:

$$\frac{1}{C_\Lambda^{kk}}\sqrt{\nu\frac{R_{kk}^{WIA}}{\epsilon_{kk}^{WIA}}} = \frac{d_b}{\sqrt{C_d \mathrm{Re}_b}} \quad \text{for } kk \in [11, 22, 33], \tag{43}$$

where C_Λ^{11}, C_Λ^{22}, and C_Λ^{33} are proportionality constants. The DNS allows direct measurement of R_{ij}^{WIA} and ϵ_{ij}^{WIA} due to the methodology developed in Sec. III. Figure 8 compares the different parts

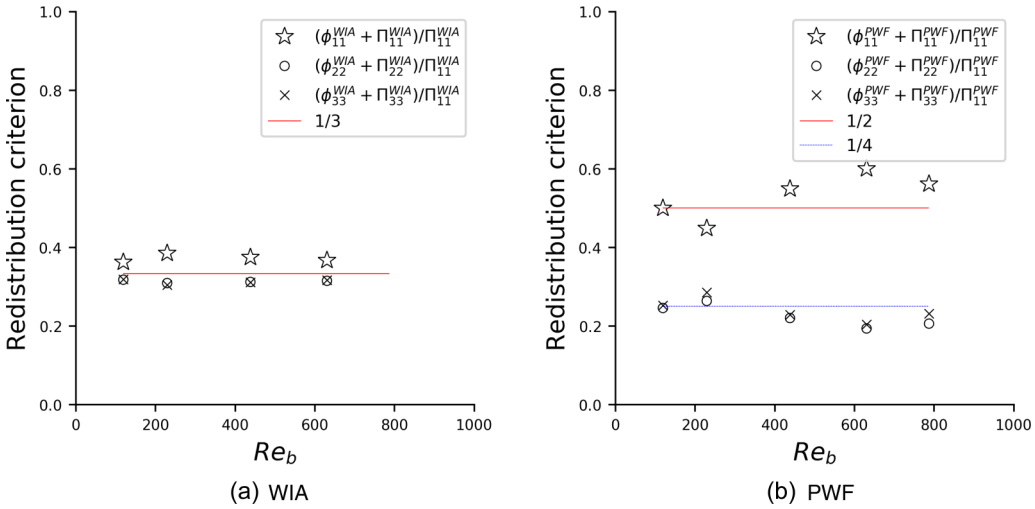

FIG. 9. Representation of the isotropy of fluctuations (redistribution + production normalized in the three directions) for WIA (a) and PWF (b). The gap between the markers and 1/3 characterizes the degree of anisotropy.

of expression (43) from DNS results (red curves). Using the drag coefficient extracted from the DNS (obtained from the balance between drag force and buoyancy: $C_d = \frac{4}{3}\frac{\alpha_v d_b(\rho_l-\rho_v)g}{\rho_l u_r^2}$), we obtain a very good agreement with expression (43). Even for low Reynolds numbers, good results are obtained. This result is surprising as it shows that the correlation used to characterize the collective instability of wakes follows a similar trend to characterize nonstationary wakes. Note that for $\mathrm{Re}_b \approx 100$, the WIA is only 7% of the kinetic energy in the liquid phase. These results are supported by experimental validation and by the theory developed in Ref. [7]. In addition, this expression works for each component of the Reynolds stresses separately with the same proportionality constants ($C_\Lambda^{11} = C_\Lambda^{22} = C_\Lambda^{33} = C_\Lambda = 1.7$). Note that the difference in the proportionality constant between the results of Ref. [17] and ours is expected. Indeed, Ref. [17] directly measures the integral length scale, while we measure $\sqrt{\nu R_{ij}^{WIA}/\epsilon_{ij}^{WIA}}$ which is proportional to this scale. The ratio between the two constants is therefore another proportionality constant.

So we write the WIA dissipation model as

$$\epsilon_{ij}^{WIA} = \frac{C_d u_r R_{ij}^{WIA}}{C_\Lambda^2 d_b}. \tag{44}$$

C. WIA redistribution

We seek to show the degree of WIA isotropy to know if a tensor model is necessary or if a scalar model would be equally effective. The redistribution phenomenon takes energy produced on the axial component (xx) and redistributes it on transversal components. Thus, to measure the degree of anisotropy of the flow, we must compare the diagonal components of the sum of production and redistribution ($\Pi_{ij} + \phi_{ij}$; see Ref. [71]). In Fig. 9 this sum normalized by the axial production is plotted on the diagonal components of the Reynolds tensor for PWF and WIA. The gap between the markers and 1/3 shows the degree of anisotropy. Even if the WIA is slightly more energetic on the axial component, the redistribution phenomenon is extremely efficient and tends towards a very strong isotropy of the WIA. The difference with the anisotropy of PWFs in Fig. 9(b) is clear. This observation confirms that the anisotropy of bubble-induced turbulence is mainly due to the anisotropy of PWFs. At first order, we can consider WIA as isotropic and model production and

redistribution together as

$$\phi_{ij}^{WIA} + \Pi_{ij}^{WIA} = \begin{pmatrix} \frac{1}{3} & 0 & 0 \\ 0 & \frac{1}{3} & 0 \\ 0 & 0 & \frac{1}{3} \end{pmatrix} \Pi_{11}^{WIA}. \tag{45}$$

D. A complete model example

Bringing together Eqs. (28), (33), (44), and (45), we get in the present configuration (namely, without diffusion of the WIA)

$$\begin{aligned} \frac{D\left(\alpha_l R_{ij}^{WIA}\right)}{Dt} &= \frac{1}{3}\delta_{ij}\alpha_v \frac{\Delta\rho}{\rho_l} g u_r \left(0.9 - e^{-\frac{\mathrm{Re}_b}{\mathrm{Re}_b^c}}\right) - 2\frac{C_d u_r R_{ij}^{WIA}}{C_\Lambda^2 d_b} \\ &= 0. \end{aligned}$$

We can then obtain an algebraic formulation for WIA Reynolds stresses at statistical equilibrium. To obtain a complete model of bubble-induced turbulence in bubbly flow, a PWF model is also required. Here we use the one developed in Ref. [16] to obtain

$$R_{ij} = R_{ij}^{WIA} + R_{ij}^{PWF}, \tag{46}$$

$$R_{ij}^{WIA} = \frac{C_\Lambda^2}{6C_d}\frac{\Delta\rho}{\rho_l}\alpha_v g d_b \left(0.9 - e^{-\frac{\mathrm{Re}_b}{\mathrm{Re}_b^c}}\right)\delta_{ij}, \tag{47}$$

$$R_{ij}^{PWF} = \alpha_v u_r^2 \begin{pmatrix} 3/20 & 0 & 0 \\ 0 & 3/20 & 0 \\ 0 & 0 & 1/5 + 3C_V/2 \end{pmatrix}. \tag{48}$$

These closures are valid for a bubbly flow without wall where the diffusion is negligible (with three homogeneous directions). The PWF model involves the contribution of the potential flow around bubbles and of the averaged wakes. The averaged wakes influence the streamwise component of the Reynolds stresses and are taken into account via the coefficient C_V for the wake volume. The constant C_V can depend on many parameters. On transversal components, the contribution of the potential flow is very low; then the Reynolds stresses are mainly dominated by the WIA contribution and by the coefficient C_Λ. These equations form a complete model of bubble-induced agitation for bubbly flows and can be tested. Knowing the impact of fixed bubbles on PWFs (see Sec. IV B), the calibration of the model must be done on free bubbles.

E. Calibration of the model on free bubbles

Differences between free and fixed bubbles have been developed in Sec. IV B. Mostly, they concern the inhomogeneity of bubble distribution and the relative motion of bubbles. The main consequence of these differences is a clear modification of the wake structure (but it has a negligible impact on WIA). In Fig. 10 the complete model for bubble-induced turbulence behaves well but only if the parameter C_Λ (characteristic of the dissipation) is changed from 1.6 (calibrated for a uniform distribution of fixed bubbles) to 2.7. Increasing C_Λ means a decrease in dissipation. The modification of the parameter is required because of the homogeneity of bubble distribution in the case of fixed bubbles (see Sec. IV B). The good trend with the Reynolds number shows that the hypothesis adopted to model the production term is correct. Moreover, the use of a constant parameter C_V independent of Re_b is enough to reproduce the numerical results.

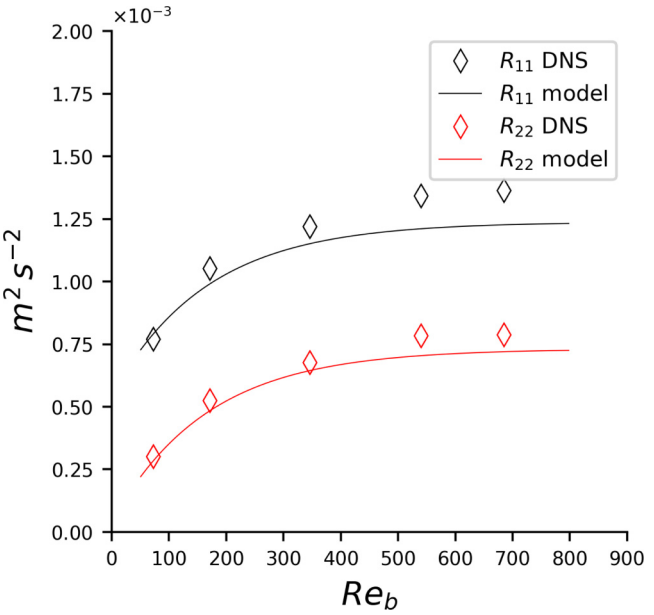

FIG. 10. Comparison between DNS of free bubbles and the complete model of bubble-induced turbulence [Eqs. (46), (47), and (48)]. Constants are $C_V = 0.36$ and $C_\Lambda = 2.7$.

Finally, the turbulence model for bubbly flows can be written in a more general context than BIA (including SIT). Taking into account the distinctions presented in the introduction (see Fig. 1):

$$R_{ij} = R_{ij}^{SIT} + R_{ij}^{FCIT} + R_{ij}^{PWF} + R_{ij}^{WIA},$$

$$\frac{DR_{ij}^{SIT}}{Dt} = D_{ij,\text{turb}}^{SIT} + D_{ij,\text{mol}}^{SIT} + P_{ij}^{SIT} - \epsilon_{ij}^{SIT} + \phi_{ij}^{SIT},$$

$$\frac{DR_{ij}^{WIA}}{Dt} = D^{WIA} + \frac{\Delta\rho}{3\rho_l}\delta_{ij}\alpha_v g u_r\left(0.9 - e^{-\frac{\text{Re}_b}{\text{Re}_b^c}}\right) - 2\frac{C_d u_r R_{ij}^{WIA}}{C_\Lambda^2 d_b},$$

$$R_{ij}^{PWF} = \alpha_v u_r^2 \begin{pmatrix} 3/20 & 0 & 0 \\ 0 & 3/20 & 0 \\ 0 & 0 & 1/5 + 3C_V/2 \end{pmatrix},$$

$$C_\Lambda = 2.7, \quad C_V = 0.36, \quad \text{Re}_b^c = 170,$$

where the diffusion of WIA D^{WIA} can possibly be estimated from the work in Ref. [11]. R_{ij}^{SIT} is the single-phase turbulence classically modeled with a Reynolds stress model [72,73] without any additional interfacial production. Reference [13] shows that the redistribution tensor ϕ_{ij}^{SIT} is disturbed by the presence of bubbles in accordance with the study of [74]. Additionally, diffusion D^{SIT} is reduced by the near-wall bubble layer. With this type of model, any kind of velocity fluctuations presented in Fig. 1 should be taken into account separately by dedicated models. As a reminder, the SIT equation contains both the SPT part and the MCIT part. Here it remains to model the term R_{ij}^{FCIT} (see [4]). This system of equations can be used in two-fluid simulations for a more consistent model of pseudoturbulence (BIA) as the two contributions for WIA and PWF are modeled by dedicated processes. It could be used either to simulate two-fluid RANS Euler-Euler (interpenetrating media) bubbly flows in conjunction with an appropriate model for CIT, or to develop multiphase turbulence models at lower computational cost than DNS in order to study FCIT. This last approach is applicable wherever there is a clean separation of scales between the

integral length scale of turbulence and the bubble diameter (as in, for instance, Wang *et al.* [75]). With the current knowledge, it is sufficient to model the trace of WIA as it has been shown to be isotropic. In more complex situations, extradiagonal components may have stronger impact.

VI. CONCLUSION

In this paper, DNS of bubbly flows have been performed to analyze velocity fluctuations and to propose a new strategy for bubble-induced agitation model development. To this end, a method to separate the transport equation of Reynolds stresses has been developed based on fixed-bubble simulations. This work starts with a distinction between the diverse origins of velocity fluctuations in the liquid, proposing a new interpretation of traditional concepts in the two-phase flows literature. Total fluctuations are divided into two categories. The first one called shear-induced turbulence (SIT) gathers all the fluctuations induced by mean velocity gradients, thus including both classical turbulent fluctuations [single-phase turbulence (SPT)] and mean cluster-induced turbulence (MCIT). In the second category, fluctuations due to two-phase intermittency are collected under bubble-induced agitation (BIA); they include the fluctuating part of cluster-induced turbulence (FCIT), the agitation resulting from wakes and their collective interactions [wake-induced agitation (WIA)], and the nonturbulent fluctuations resulting from averaged wakes and potential flows around bubbles [potential flow and averaged wake fluctuations (PWFs)].

In this work, our attention is set on homogeneous bubbly flows where CIT is negligible based on DNS with a void fraction $\alpha = 6\%$. Our goal is to make progress in the understanding of the repartition between WIA and PWFs and to better model their interactions. To do so, we compare freely evolving bubbles at bubble Reynolds numbers ranging from 100 to 800 to their counter-part where bubbles are rendered motionless with an external artificial force. Flow dynamics have been discussed to understand, in particular, the differences observed between fixed-bubble and free-bubble simulations. It has been shown that fixing bubbles has a significant influence on PWFs, while WIA is very similar between free-bubble and fixed-bubble cases. The statistical analysis confirmed the good quality of the results concerning WIA. Moreover, the signature of an energy conversion from wake kinetic energy (PWF) to turbulent kinetic energy (WIA) has been observed. It shows the importance of nonlinear interactions and transfers between PWFs and WIA. Then, the simulations have been used to propose an algebraic closure of WIA based on the different terms of its transport equation. This model was extended to total fluctuations for freely evolving bubbles. The results are encouraging and allow accurate predictions on our database over a wide range of bubble Reynolds numbers. The strategy is complete and can be used for two-phase BIA model development. Due to its mechanistic construction, the validity domain is expected to be wider than the range of dimensionless numbers on which it has been created, in particular on the range of void fractions as long as the flow regime is dispersed bubbles ($\alpha \in [0, 0.3]$). The model is theoretically suited for any Reynolds number, but we do not expect a clear influence on high Reynolds flows ($\mathrm{Re}_L = U_L D_h/\nu_L > 100\,000$ on the liquid phase, based on the liquid bulk velocity U_L and hydraulic diameter D_h), in which the SPT part will be much larger than the BIA fluctuations (and therefore where a more classical model would give similar results). On the other hand, in low Reynolds number flows (pool boiling, liquid at rest, low convection), BIA contribution (and its subparts PWF and WIA) seems necessary. However, there are still some limitations:

(1) The WIA model has been developed from calculations in tri-periodic bubbly flow without walls. Therefore, nondiagonal components of WIA Reynolds stresses are null. It is likely that the presence of wall redistributes a part of the energy on the cross-correlation. This is challenging to study, because it requires the analysis of WIA in the case of a channel, but in that configuration we cannot separate WIA from single-phase turbulence in the current state of knowledge.

(2) PWF and WIA models require additional validation with numerical simulations. The dependence of the model on the void fraction or on the bubble deformation must be investigated further. More experimental validation would also be welcome.

(3) CIT is not addressed in this work. It should be considered in the future. It is an important prospect for future studies.

(4) The impact of bubble clustering on the PDFs requires further study, for instance, by using local bubble volume fraction.

(5) Following Wang *et al.* [75], the measurement of the particle-fluid-particle stress tensor could be assessed on our DNS, by separating the interaction of particles between themselves, from the interaction of a particle with the "undisturbed" flow.

Raw data were generated at the CINES large-scale facility. Derived data supporting the findings of this study are available from the corresponding author upon reasonable request.

ACKNOWLEDGMENTS

The authors would like to thank Prof. F. Risso for sharing his expertise in this area. The authors also would like to convey their sincere thanks to GENCI(Grand Équipement National de Calcul Intensif) and the TGCC (Très Grand Centre de calcul du CEA) for providing the necessary computational resources for performing the DNS calculations. This work was granted access to the HPC resources of CINES under the allocations A0042b7712, A0062b7712, and A0102b7712 made by GENCI. Also, we would like to acknowledge the CEA/DEN for the HPC ressources allocated on COBALT and CURIE supercomputers at TGCC.

[1] M. Lance and J. Bataille, Turbulence in the liquid phase of a uniform bubbly air-water flow, J. Fluid Mech. **222**, 95 (1991).

[2] F. Risso, V. Roig, Z. Amoura, G. Riboux, and A. M. Billet, Wake attenuation in large Reynolds number dispersed two-phase flows, Philos. Trans. R. Soc. A **366**, 2177 (2008).

[3] A. Rasam, Anisotropy-resolving subgrid-scale modelling using explicit algebraic closures for large eddy simulation, Ph.D. thesis, KTH Royal Institute of Technology, 2014.

[4] N. Panicker, A. Passalacqua, and R. O. Fox, Computational study of buoyancy driven turbulence in statistically homogeneous bubbly flows, Chem. Eng. Sci. **216**, 115546 (2020).

[5] B. Gvozdić, O.-Y. Dung, E. Alméras, D. P. van Gils, D. Lohse, S. G. Huisman, and C. Sun, Experimental investigation of heat transport in inhomogeneous bubbly flow, Chem. Eng. Sci. **198**, 260 (2019); B. Gvozdić, E. Alméras, V. Mathai, X. Zhu, D. P. M. van Gils, R. Verzicco, S. G. Huisman, C. Sun, and D. Lohse, J. Fluid Mech **845**, 226 (2018).

[6] A. Shaikh and M. H. Al-Dahhan, A review on flow regime transition in bubble columns, Int. J. Chem. Reactor Eng. **5**, 1 (2007).

[7] F. Risso, Agitation, mixing, and transfers induced by bubbles, Annu. Rev. Fluid Mech. **50**, 25 (2018).

[8] G. Riboux and D. Legendre, A model of bubble-induced turbulence based on large-scale wake interactions, J. Fluid Mech. **719**, 362 (2013).

[9] M. C. Baker, R. O. Fox, B. Kong, J. Capecelatro, and O. Desjardins, Reynolds-stress modeling of cluster-induced turbulence in particle-laden vertical channel flow, Phys. Rev. Fluids **5**, 074304 (2020).

[10] C. Colin, J. Fabre, and A. Kamp, Turbulent bubbly flow in pipe under gravity and microgravity conditions, J. Fluid Mech. **711**, 469 (2012).

[11] E. Alméras, V. Mathai, D. Lohse, and C. Sun, Experimental investigation of the turbulence induced by a bubble swarm rising within incident turbulence, J. Fluid Mech. **825**, 1091 (2017).

[12] M. Cisse, E.-W. Saw, M. Gibert, E. Bodenschatz, and J. Bec, Turbulence attenuation by large neutrally buoyant particles, Phys. Fluids **27**, 061702 (2015).

[13] A. du Cluzeau, G. Bois, and A. Toutant, Analysis and modeling of Reynolds stresses in turbulent bubbly up-flows from direct numerical simulations, J. Fluid Mech. **866**, 132 (2019).

[14] E. Bouche, V. Roig, and F. Risso, Homogeneous swarm of high-Reynolds-number bubbles rising within a thin gap. Part 1: Bubble dynamics, J. Fluid Mech. **704**, 211 (2012).

[15] E. Bouche, V. Roig, and F. Risso, Homogeneous swarm of high-Reynolds-number bubbles rising within a thin gap. Part 2: Liquid dynamics, J. Fluid Mech. **758**, 508 (2014).
[16] F. Risso, Physical interpretation of probability density functions of bubble-induced agitation, J. Fluid Mech. **809**, 240 (2016).
[17] Z. Amoura, C. Besnaci, and F. Risso, Velocity fluctuations generated by the flow through a random array of spheres: A model of bubble-induced agitation, J. Fluid Mech. **823**, 592 (2017).
[18] M. Colombo and M. Fairweather, Multiphase turbulence in bubbly flows: RANS simulations, Int. J. Multiphase Flow **77**, 222 (2015).
[19] S. Hosokawa and A. Tomiyama, Bubble-induced pseudo turbulence in laminar pipe flows, Int. J. Heat Fluid Flow **40**, 97 (2013).
[20] A. Vaidheeswaran and T. Hibiki, Bubble-induced turbulence modeling for vertical bubbly flows, Int. J. Heat Mass Transf. **115**, 741 (2017).
[21] C. Morel, *Mathematical Modeling of Two-Phase Flow* (Springer, Stuttgart, Germany, 2015).
[22] G. Bois, Direct numerical simulation of a turbulent bubbly flow in a vertical channel: Towards an improved second-order Reynolds stress model, Nucl. Eng. Des. **321**, 92 (2017).
[23] J. Chahed, V. Roig, and L. Masbernat, Eulerian-Eulerian two-fluid model for turbulent gas-liquid bubbly flows, Int. J. Multiphase Flow **29**, 23 (2003).
[24] K. Haase, U. D. Kück, J. Thöming, and C. J. Kähler, Emulation of bubble-induced turbulence using randomly moving particles in a grid structure, Chem. Eng. Technol. **40**, 1502 (2017).
[25] A. W. Vreman and J. G. Kuerten, Turbulent channel flow past a moving array of spheres, J. Fluid Mech. **856**, 580 (2018).
[26] A. Loisy, A. Naso, and P. D. Spelt, The effective diffusivity of ordered and freely evolving bubbly suspensions, J. Fluid Mech. **840**, 215 (2018).
[27] M. Ilić, Statistical analysis of liquid phase turbulence based on direct numerical simulations of bubbly flows, Forschungszentrum Karlsruhe. Forschungszentrum Karlsruhe in der Helmholtz-Gemeinschaftt Wissenschaftliche Berichte FZKA 7199, Ph.D. thesis, 2006.
[28] S. Hosokawa, T. Suzuki, and A. Tomiyama, Turbulence kinetic energy budget in bubbly flows in a vertical duct, Exp. Fluids **52**, 719 (2012).
[29] C. Santarelli, J. Roussel, and J. Fröhlich, Budget analysis of the turbulent kinetic energy for bubbly flow in a vertical channel, Chem. Eng. Sci. **141**, 46 (2016).
[30] I. Kataoka and A. Serizawa, Basic equations of turbulence in gas-liquid two-phase flow, Int. J. Multiphase Flow **15**, 843 (1989).
[31] A. Fujiwara, D. Minato, and K. Hishida, Effect of bubble diameter on modification of turbulence in an upward pipe flow, Int. J. Heat Fluid Flow **25**, 481 (2004).
[32] M. E. Shawkat and C. Y. Ching, Liquid turbulence kinetic energy budget of co-current bubbly flow in a large diameter vertical pipe, J. Fluids Eng. **133**, 091303 (2011).
[33] D. Izbassarov, Z. Ahmed, P. Costa, V. Vuorinen, O. Tammisola, and M. Muradoglu, Polymer drag reduction in surfactant-contaminated turbulent bubbly channel flows, Phys. Rev. Fluids **6**, 104302 (2021).
[34] T. Ma, C. Santarelli, T. Ziegenhein, D. Lucas, and J. Fröhlich, Direct numerical simulation-based Reynolds-averaged closure for bubble-induced turbulence, Phys. Rev. Fluids **2**, 034301 (2017).
[35] T. Ma, D. Lucas, and A. D. Bragg, Explicit algebraic relation for calculating Reynolds normal stresses in flows dominated by bubble-induced turbulence, Phys. Rev. Fluids **5**, 084305 (2020).
[36] J. Capecelatro, O. Desjardins, and R. Fox, Strongly coupled fluid-particle flows in vertical channels. I. Reynolds-averaged two-phase turbulence statistics. Phys. Fluids **28**, 033306 (2016).
[37] J. Capecelatro, O. Desjardins, and R. Fox, Strongly coupled fluid-particle flows in vertical channels. II. Turbulence modeling. Phys. Fluids **28**, 033307 (2016).
[38] Y. Liao, T. Ma, E. Krepper, D. Lucas, and J. Fröhlich, Application of a novel model for bubble-induced turbulence to bubbly flows in containers and vertical pipes, Chem. Eng. Sci. **202**, 55 (2019).
[39] A. Innocenti, A. Jaccod, S. Popinet, and S. Chibbaro, Direct numerical simulation of bubble-induced turbulence, J. Fluid Mech. **918**, A23 (2021).

[40] S. Erdogan, T. Schulenberg, O. Deutschmann, and M. Worner, Evaluation of models for bubble-induced turbulence by DNS and utilization in two-fluid model computations of an industrial pilot-scale bubble column, Chem. Eng. Res. Design **175**, 283 (2021).
[41] Y. Sato and K. Sekoguchi, Liquid velocity distribution in two-phase bubble flow, Int. J. Multiphase Flow **2**, 79 (1975).
[42] S. Tenneti, R. Garg, C. M. Hrenya, R. O. Fox, and S. Subramaniam, Direct numerical simulation of gas-solid suspensions at moderate Reynolds number: Quantifying the coupling between hydrodynamic forces and particle velocity fluctuations, Powder Technol. **203**, 57 (2010).
[43] L. V. Wijngaarden, On pseudo turbulence, Theor. Comput. Fluid Dyn. **10**, 449 (1998).
[44] R. O. Fox, On multiphase turbulence models for collisional fluid-particle flows, J. Fluid Mech. **742**, 368 (2014).
[45] V. Pandey, R. Ramadugu, and P. Perlekar, Liquid velocity fluctuations and energy spectra in three-dimensional buoyancy-driven bubbly flows, J. Fluid Mech. **884**, R6 (2020).
[46] E. Manon, Contribution à l'analyse et à la modélisation locale des écoulements bouillants sous-saturés dans les conditions des Réacteurs à Eau sous Pression, Ph.D. thesis, Ecole Centrale Paris, 2000.
[47] See, https://webbook.nist.gov/chemistry/fluid.
[48] B. Mathieu, Etudes physique, expérimentale et numérique des mécanismes de base intervenant dans les écoulements diphasiques en micro-fluidique, Ph.D. thesis, Polytech Marseille - Université de Provence, 2003.
[49] I. Kataoka, Local instant formulation of two-phase flow, Int. J. Multiphase Flow **12**, 745 (1986).
[50] G. Tryggvason, B. Bunner, A. Esmaeeli, and N. Al-Rawahi, Computations of multiphase flows, Adv. Appl. Mech. **39**, 81 (2003).
[51] E. G. Puckett, A. S. Almgren, J. B. Bell, D. L. Marcus, and W. J. Rider, A high-order projection method for tracking fluid interfaces in variable density incompressible flows, J. Comput. Phys. **130**, 269 (1997).
[52] J. H. Williamson, Low-storage Runge-Kutta schemes, J. Comput. Phys. **35**, 48 (1980).
[53] A. Toutant, Modélisation physique des interactions entre interfaces et turbulence, Ph.D. thesis, Institut National Polytechnique de Toulouse, 2006.
[54] G. Bois, G. Fauchet, and A. Toutant, DNS of a turbulent steam/water bubbly flow in a vertical channel, in *Proceedings of the 9th International Conference on Multiphase Flows (ICMF2016)*, ICMF (2016), 323263.
[55] G. Bois, A. du Cluzeau, A. Toutant, and J.-M. Martinez, DNS of turbulent bubbly flows in plane channels using the Front-Tracking algorithm of TrioCFD, in *Fluids Engineering Division Summer Meeting* (American Society of Mechanical Engineers, 2017), p. V01CT16A005.
[56] A. Toutant, E. Labourasse, O. Lebaigue, and O. Simonin, DNS of the interaction between a deformable buoyant bubble and a spatially decaying turbulence: *A priori* tests for LES two-phase flow modelling, Comput. Fluids **37**, 877 (2008).
[57] A. Toutant, M. Chandesris, D. Jamet, and O. Lebaigue, Jump conditions for filtered quantities at an under-resolved discontinuous interface. Part 1: Theoretical development. Int. J. Multiphase Flow **35**, 1100 (2009).
[58] A. Toutant, B. Mathieu, and O. Lebaigue, Volume-conserving mesh smoothing for front-tracking methods, Comput. Fluids **67**, 16 (2012).
[59] A. du Cluzeau, G. Bois, A. Toutant, and J. M. Martinez, On bubble forces in turbulent channel flows from direct numerical simulations, J. Fluid Mech. **882**, A27 (2020).
[60] A. du Cluzeau, G. Bois, and A. Toutant, Modelling of the laminar dispersion force in bubbly flows from direct numerical simulations, Phys. Fluids **32**, 012106 (2020).
[61] M. Chandesris and D. Jamet, Boundary conditions at a planar fluid-porous interface for a Poiseuille flow, Int. J. Heat Mass Transf. **49**, 2137 (2006).
[62] M. Chandesris and D. Jamet, Derivation of jump conditions for the turbulence k-ϵ model at a fluid/porous interface, Int. J. Heat Fluid Flow **30**, 306 (2009).
[63] M. Chandesris, A. D'Hueppe, B. Mathieu, D. Jamet, and B. Goyeau, Direct numerical simulation of turbulent heat transfer in a fluid-porous domain, Phys. Fluids **25**, 125110 (2013).

[64] D. Dupuy, A. Toutant, and F. Bataille, Turbulence kinetic energy exchanges in flows with highly variable fluid properties, J. Fluid Mech. **834**, 5 (2018).
[65] A. M. Thomas, J. Fang, J. Feng, and I. A. Bolotnov, Estimation of shear-induced lift force in laminar and turbulent flows, Nuclear Tech. **190**, 274 (2015).
[66] J. Jeong and F. Hussain, On the identification of a vortex, J. Fluid Mech. **285**, 69 (1995).
[67] See, http://triocfd.cea.fr/Pages/Research_directions/FT_database.aspx.
[68] L. Schiller and A. Naumann, Über die grundlegenden Berechnungen bei der Schwerkraftaufbereitung, Z. Vereines Deutscher Inge. **77**, 318 (1933).
[69] V. N. Prakash, J. Martínez-mercado, L. V. Wijngaarden, E. Mancilla, Y. Tagawa, D. Lohse, and C. Sun, Energy spectra in turbulent bubbly flows, J. Fluid Mech. **791**, 174 (2016).
[70] G. Riboux, Hydrodynamique d'un essaim de bulles en ascension, Ph.D. thesis, Toulouse, INPT, 2007.
[71] T. Ma, D. Lucas, S. Jakirlc, and J. Frohlich, Progress in the second-moment closure for bubbly flow based on direct numerical simulation data, J. Fluid Mech. **883**, A9 (2019).
[72] B. E. Launder, G. J. Reece, and W. Rodi, Progress in the development of a Reynolds-stress turbulence closure, J. Fluid Mech. **68**, 537 (1975).
[73] C. G. Speziale, S. Sarkar, and T. B. Gatski, Modelling the pressure-strain correlation of turbulence: An invariant dynamical systems approach, J. Fluid Mech. **227**, 245 (1991).
[74] M. Lance, J. L. Marie, and J. Bataille, Homogeneous turbulence in bubbly flows, J. Fluids Eng. **113**, 295 (1991).
[75] M. Wang, Y. Yang, D. Z. Zhang, and S. Balachandar, Numerical calculation of the particle-fluid-particle stress in random arrays of fixed particles, Phys. Rev. Fluids **6**, 104306 (2021).